Volume 9 • Issue 2 • March / April 2015

Editor-in-Chief
Professor Hu, Yu-Chen

INTERNATIONAL JOURNAL OF

IMAGE PROCESSING (IJIP)

ISSN : 1985-2304

Publication Frequency: 6 Issues Per Year

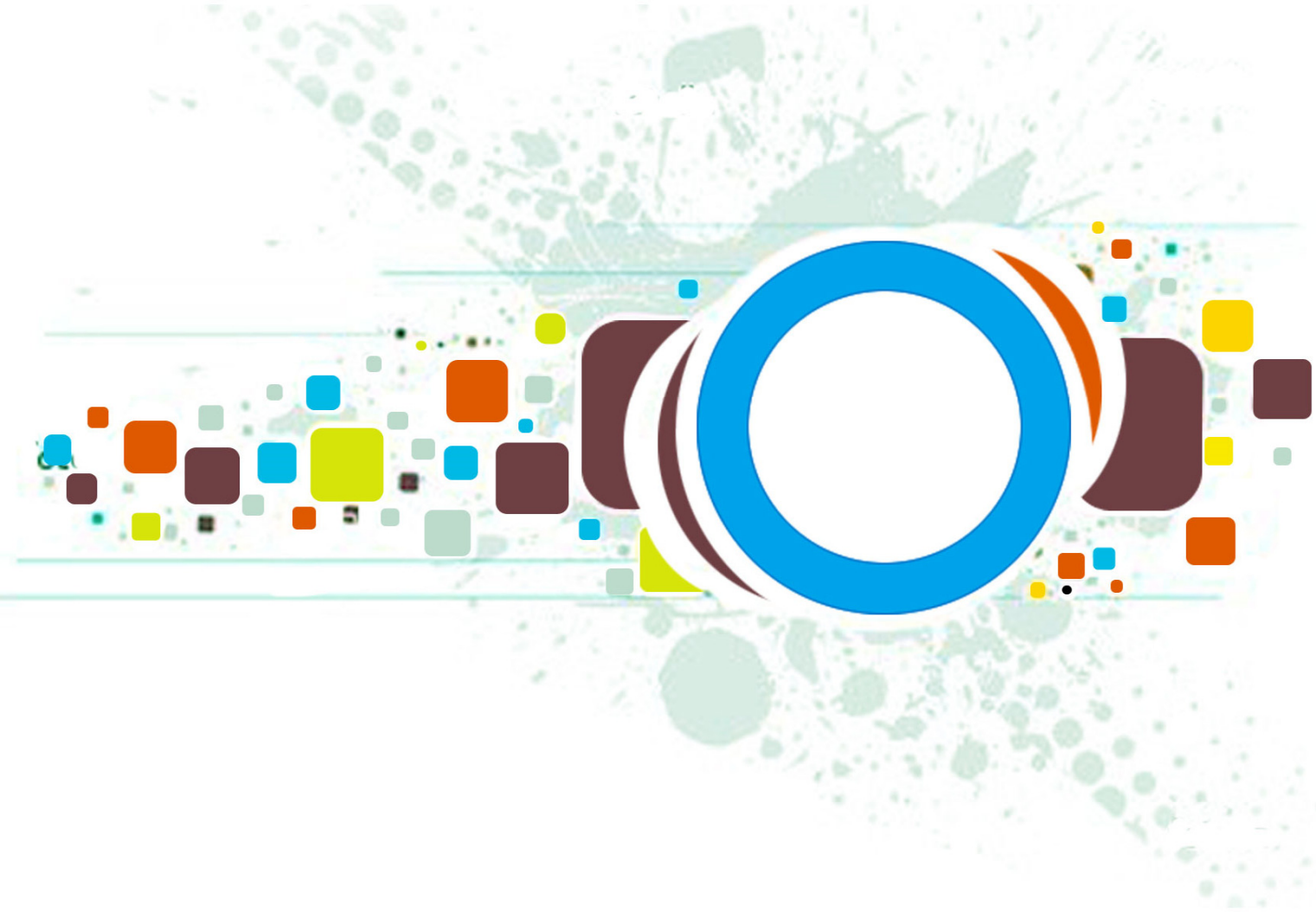

CSC PUBLISHERS
http://www.cscjournals.org

INTERNATIONAL JOURNAL OF IMAGE PROCESSING (IJIP)

VOLUME 9, ISSUE 2, 2015

EDITED BY
DR. NABEEL TAHIR

ISSN (Online): 1985-2304

International Journal of Image Processing (IJIP) is published both in traditional paper form and in Internet. This journal is published at the website http://www.cscjournals.org, maintained by Computer Science Journals (CSC Journals), Malaysia.

IJIP Journal is a part of CSC Publishers

Computer Science Journals

http://www.cscjournals.org

INTERNATIONAL JOURNAL OF IMAGE PROCESSING (IJIP)

Book: Volume 9, Issue 2, March / April 2015
Publishing Date: 30-04-2015
ISSN (Online): 1985-2304

IJIP Journal is a part of CSC Publishers
http://www.cscjournals.org

Published in Malaysia

Typesetting: Camera-ready by author, data conversation by CSC Publishing Services – CSC Journals, Malaysia

CSC Publishers, 2015

EDITORIAL PREFACE

The International Journal of Image Processing (IJIP) is an effective medium for interchange of high quality theoretical and applied research in the Image Processing domain from theoretical research to application development. This is the *Second* Issue of Volume *Nine* of IJIP. The Journal is published bi-monthly, with papers being peer reviewed to high international standards. IJIP emphasizes on efficient and effective image technologies, and provides a central for a deeper understanding in the discipline by encouraging the quantitative comparison and performance evaluation of the emerging components of image processing. IJIP comprehensively cover the system, processing and application aspects of image processing. Some of the important topics are architecture of imaging and vision systems, chemical and spectral sensitization, coding and transmission, generation and display, image processing: coding analysis and recognition, photopolymers, visual inspection etc.

The initial efforts helped to shape the editorial policy and to sharpen the focus of the journal. Started with Volume 9, 2015, IJIP appears with more focused issues. Besides normal publications, IJIP intends to organize special issues on more focused topics. Each special issue will have a designated editor (editors) – either member of the editorial board or another recognized specialist in the respective field.

IJIP gives an opportunity to scientists, researchers, engineers and vendors from different disciplines of image processing to share the ideas, identify problems, investigate relevant issues, share common interests, explore new approaches, and initiate possible collaborative research and system development. This journal is helpful for the researchers and R&D engineers, scientists all those persons who are involve in image processing in any shape.

Highly professional scholars give their efforts, valuable time, expertise and motivation to IJIP as Editorial board members. All submissions are evaluated by the International Editorial Board. The International Editorial Board ensures that significant developments in image processing from around the world are reflected in the IJIP publications.

IJIP editors understand that how much it is important for authors and researchers to have their work published with a minimum delay after submission of their papers. They also strongly believe that the direct communication between the editors and authors are important for the welfare, quality and wellbeing of the Journal and its readers. Therefore, all activities from paper submission to paper publication are controlled through electronic systems that include electronic submission, editorial panel and review system that ensures rapid decision with least delays in the publication processes.

To build its international reputation, we are disseminating the publication information through Google Books, Google Scholar, Directory of Open Access Journals (DOAJ), Open J Gate, ScientificCommons, Docstoc and many more. Our International Editors are working on establishing ISI listing and a good impact factor for IJIP. We would like to remind you that the success of our journal depends directly on the number of quality articles submitted for review. Accordingly, we would like to request your participation by submitting quality manuscripts for review and encouraging your colleagues to submit quality manuscripts for review. One of the great benefits we can provide to our prospective authors is the mentoring nature of our review process. IJIP provides authors with high quality, helpful reviews that are shaped to assist authors in improving their manuscripts.

Editorial Board Members
International Journal of Image Processing (IJIP)

EDITORIAL BOARD

TABLE OF CONTENTS

Volume 9, Issue 2, March / April 2015

Pages

Steganography using Coefficient Replacement and Adaptive Scaling based on DTCWT

N Sathisha *nsathisha@gmail.com*
Department of ECE,
Govt. S K S J Technological Institute,
Bangalore, India.

K Suresh Babu *ksb1559@gmail.com*
Department of ECE,
University Visvesvaraya College of Engineering,
Bangalore, India.

K B Raja *raja_kb@yahoo.com*
Department of ECE,
University Visvesvaraya College of Engineering,
Bangalore, India.

K R Venugopal *venugopalkr@gmail.com*
Principal,
University Visvesvaraya College of Engineering,
Bangalore, India.

Abstract

Steganography is an authenticated technique for maintaining secrecy of embedded data. Steganography provides hardness of detecting the hidden data and has a potential capacity to hide the existence of confidential data. In this paper, we propose a novel steganography using coefficient replacement and adaptive scaling based on Dual Tree Complex Wavelet Transform (DTCWT) technique. The DTCWT and LWT 2 is applied on cover image and payload respectively to convert spatial domain into transform domain. The HH sub band coefficients of cover image are replaced by the LL sub band coefficients of payload to generate intermediate stego object and the adaptive scaling factor is used to scale down intermediate stego object coefficient values to generate final stego object. The adaptive scaling factor is determined based on entropy of cover image. The security and the capacity of the proposed method are high compared to the existing algorithms.

Keywords: Steganography, DTCWT, LWT, Stego Image, Cover Image, Adaptive Scaling, Entropy.

1. INTRODUCTION

Enormous growth of high speed computer networks and internet communication leads to increase in demand of data security systems. The various data hiding techniques for providing security to the confidential information are cryptography, watermarking and steganography. Cryptography scrambles the data to prevent the attacker from understanding the contents. Watermarking is to hide signal into host signal for marking the host signal to be one's legal property. Steganography is the technique of embedding confidential information in a carrier medium the carrier medium can be images, audio, video and text files. Digital images are the most commonly used carrier media used for steganography. The Graphics Interchange Format (GIF), Joint Photographic Experts Group (JPEG) format and Portable Network Graphics (PNG)

formats are the most popular image file formats being used for images shared on internet. Steganographic techniques which are used to modify image files for hiding information includes spatial domain technique, transform domain technique, spread spectrum technique, adaptive technique, statistical methods and distortion techniques. In spatial domain technique, the secret messages are embedded directly. The most common and simplest steganography method is the Least Significant Bit (LSB) insertion method. In the LSB technique the LSB bits of the cover image pixels are replaced by the secret information message bits which are permuted before embedding. A basic classification of spatial domain steganographic algorithms are (i) non filtering algorithm (ii) randomised algorithms and (iii) filtering algorithms. In transform domain technique the cover image is converted into transform domain by applying transformation such as Discrete Cosine Transform (DCT), Discrete Wavelet Transform (DWT), Integer Wavelet Transform (IWT), Discrete Fourier Transform (DFT), Fast Fourier Transform (FFT) etc., and then embedding of confidential information into these transformed coefficients of the cover image. The wavelet transform separates the high frequency and low frequency information on a pixel by pixel basis. DWT is preferred over DCT because image in low frequency at various levels can offer high resolution. The DWT is decomposed into Approximation band (LL), vertical band (LH), horizontal band (HL) and diagonal detail band (HH). The approximation band consists of low frequency wavelet coefficients which contain significant part of the spatial domain image. The other bands also called as detail bands consists of high frequency coefficients which contains the insignificant part and edge details of the spatial domain image. DWT will allow independent processing without significant perceptible interaction between them and hence making the process imperceptibility with more effective. Applications of steganography are in digital copy right protection, digital media content surveillance, content authentication and covert communication involving industries like e-pressing, e-government, e-business etc.,

Contributions: In this paper steganography using coefficient replacement and adaptive scaling based on DTCWT technique is proposed. The DTCWT and LWT are applied on cover and payload images respectively. The HH coefficients of DTCWT are replaced completely by LL coefficients of LWT to generate intermediate stego object. The coefficient of intermediate stego object is scaled down by scaling factors based on the entropy of cover image to generate final stego object. The stego image is obtained by using IDTCWT on final stego object.

2. RELATED WORK

Rigdas and Themrichon Tuithung [1] proposed a Huffman encoding steganography. The Huffman encoding is applied on secret image and each bit of Huffman code of secret image is embedded into the cover image altering the LSB of each cover image pixel. Najeena and Imran [2] presented a steganographic and cryptographic technique based on chaotic encryption with adaptive pixel pair matching. The scrambled data is embedded into the cover media based on pixel pair matching technique. The cover pixel pairs are changed randomly by using keys to increase the security level of the system. Ran-zan wang and Yeh-shun chen [3] presented a steganography technique based on two way block matching procedure. The block matching procedure search for the highest similarity block from a series of blocks generated from the cover image and embeds the secret information in imperceptible areas of the cover image. The hop embedded scheme is used which resulted in high quality of stego image and extracted secret image. This method exhibits high payload embedding. Vojtech holub and Jessica fridrich [4] developed an adaptive steganographic distortion function a bank of directional high pass filters is employed to obtain the directional residuals. The impact of embedding on the every directional residual is measured. The embedding is done on smooth areas along edges and noisy areas. Baolong Guo et al., [5] proposed robust image watermarking schemes based on the mean quantization using DTCWT. The energy map of the original image is first composed from the six high frequency sub bands of DTCWT and the watermark is embedded into the high energy pixels. The two schemes embed the watermark into the high frequency and low frequency DTCWT coefficients by quantizing.

Ajit danti and Manjula [6] proposed an image steganography using DWT and hybrid wavelet transform. The cover and secret images are normalized and the wavelet coefficients are obtained

by applying DWT. The wavelet coefficients of both the cover and secret images are fused into single image. Jani Anbarasi and kannan [7] have developed a secure steganographic system for secret color image sharing with reversible characteristics. The secret color image pixels are transformed into M-ary notational system. Reversible polynomial function is generated using (t-1) digits of secret color image pixels and the secret shares are generated using reversible polynomial function and the participant's numerical key. The secret image and cover image are embedded together to construct stego image. Reversible image sharing process is used for reconstructing secret image and cover image. Secret is obtained by Lagrange's formula generated from sufficient secret shares. Quantization process is applied to improve quality of cover image. Sathya et al., [8] discussed the various techniques for data hiding in audio signal, video signal, text and JPEG images. The pros and cons of the available techniques are analysed and proposes a technique based on T-codes. T-codes are used for encoding of original message and entropy encoding of compressed stego image. After this SB technique is used for embedding process. T-codes are considered because of its self synchronizing property which increases robustness of the technique. Zawawi et al., [9] discusses the operation of active warden and how it is the main hindrance for steganography information retrieval. Active wardens are attackers of steganography which aims to destroy the possible hidden information within the carrier. If the objective of the attacker is is to disrupt the communication of hidden information then active approach will be the preferred method compared to time consuming passive steganalysis methods. Yang et al., [10] proposed an improved method of image sharing with steganography for providing authentication to prevent cheating. Manipulation of the stego images are prevented by using Hash function with secret keys. The authentication is provided by hashing 4 pixel blocks, block ID and image ID. The quality of both stego image and secret image are improved by a new arrangement of seventeen bits in the four pixel square block. Chiang- Lung Liu and Shiang-Rong Liao [11] have developed a high performance steganographic scheme for JPEG using complementary embedding strategy to avoid detections of several statistical attacks in spatial domain. Here instead of flipping the LSBs of the DCT coefficients, the secret bits are embedded in the cover image by subtracting one or adding one to the non zero DCT coefficient and hence cannot be detected by both Chi square and Extended Chi square attacks. Manjunatha Reddy and Raja [12] have proposed high capacity and security steganography using DWT technique. The wavelet coefficients of both the cover and payload are fused into single image using embedding strength alpha and beta. The cover and payload are preprocessed to reduce pixel range ensuring accurate recovery of payload at destination.

ShivaKumar et al., [13] have developed hybrid domain in LSB steganography technique which is an integration of both spatial and transform domain techniques. The cover image and payload is divided into two cells and cell I is transformed to frequency domain using DCT/DWT/FFT while maintaining components of cell II in spatial domain itself. Next, the MSB pixels of payload cell I and cell II are embedded into corresponding cell I and cell II of cover image. Youngran Park et al., [14] proposed a method for integrity verification of secret information in image steganography. The secret information is hidden into spatial domain of digital image and the embedded secret information is randomly permuted to achieve confidentiality. Integrity of secret information is verified using DCT coefficients. Xinpeng Zhang and ShouZhang Wang [15] have suggested an improvement for PVD steganography technique to reduce its vulnerability for histogram analysis there by providing enhanced security. The method preserves the advantage of low visual distortion of the PVD. This introduces a pseudo-random dithering to the division of ranges of PVDs. The Histogram based steganalysis is defeated while preserving embedding capacity and high invisibility of original PVD. Chin-Chan Chang and Hsian-Wen Tseng [16] have proposed a steganographic method which provides larger embedding capacity and minimizes the distortion of stego image. The method exploits the correlation between neighboring pixels to estimate the degree of smoothness or contrast of pixels and the pixel in the edge area has more data than those in the non edge areas. Two sided, three sided and four sided match methods are used for embedding. Manjunatha Reddy and Raja [17] proposed a wavelet based non LSB steganography technique in which the cover image is segmented into 4*4 cells and DWT/IWT is applied to each cell. The 2*2 cell of HH band of DWT/IWT are considered and manipulated with payload bit pairs using identity matrix to generate stego image and the key is used to extract payload bit pairs at

the destination. The algorithm cannot be detected by steganalysis techniques such as Chi-square and pair of values techniques.

Shiva Kumar et al., [18] proposed a bit length replacement steganography based on DCT coefficients where the cover image is segmented into smaller matrix of size 8*8 blocks and converted into DCT domain by applying 2D-DCT to each block. The MSB bits of payload are embedded into each DCT coefficients of cover image based on the coherent length 'L' which is determined by the DCT coefficient values. K.B. Shiva Kumar et al., [19] proposed a steganographic technique based on payload transformation which is a non LSB and non transform domain technique. The cover image is segmented into 2*2 matrices then the matrix for payload embedding process is obtained based on the threshold value fixed by adjacent pixel intensity differences. The transformation matrix is obtained by considering the identity matrix and the payload bit pair. The stego image matrices of size 2*2 are derived from the 2*2 cover image matrices and the transformation matrix. Key is generated with first bit payload matrix at sending end and this is used to extract the payload from stego image.

Manjunatha Reddy and Raja [20] developed wavelet based secure steganography with scrambled payload. It is a hybrid domain technique. Daubechies Lifting Wavelet Transform (LWT) is applied on the cover image whose XD band is decomposed into upper and lower bands for payload embedding. The payload is segmented into four blocks and Haar LWT is applied on alternate blocks of payload to generate F1 and F2 wavelet transform bands. The remaining blocks of payload are retained in spatial domain say S1 and S2. Then, bit reversal is applied on each coefficient of payload blocks to scramble payload and cube root is applied on these scrambled values to scale down the number of coefficient bits. The payload is embedded into XD band of cover image to obtain stego image. Arnab Kumar Maji et al., [21] proposed a steganographic scheme using Sudoku puzzle. An 18 x 18 Sudoku reference matrix is used for message embedding and 8 x 8 Sudoku is embedded into the cover image to detect whether cover image is modified or not. The secret information is embedded inside the cover image using 18 x 18 Sudoku reference matrix. In the proposed work an 18 x 18 Sudoku reference matrix is used instead of 256 x 256 or 27 x 27 reference matrix. Rashedul islam et al., [22] proposed a steganography technique to hide large data in bit map image using filtering based algorithm. The secret message is converted into cipher text using AES cryptography and the cipher text is embedded into the cover image. The method uses the concept of status checking for insertion and retrieval of message. Chi Yuan Lin et al., [23] presented a steganographic system for Vector Quantization (VQ) code books using section based informed embedding. The Fuzzy Competitive Learning Network (FCLN) clustering technology generate optimal code book for VQ. The VQ code book of secret image information is embedded into the cover image by a section based informed embedding scheme.

3. PROPOSED MODEL

In this section definitions of evaluation parameters and block diagram of proposed model are discussed.

3.1 Definitions

I *Mean Square Error (MSE):* It is defined as the square of error between two images and is calculated using Equation 1.

$$MSE = \left[\frac{1}{N}\right]^2 \sum_{i=1}^{N} \sum_{j=1}^{N} \left(X_{ij} - \overline{X}_{ij}\right)^2 \qquad (1)$$

Where N: Size of the image.

X_{ij} : The value of the pixel intensity in the cover image/original payload.

$\overline{X}_{ij}$: The value of the pixel in the stego image/extracted payload.

II *Peak Signal to Noise Ratio (PSNR):* It is the measure of quality of the image by comparing two images, i.e. it measures the percentage of the stegano data to the image percentage. PSNR is calculated using Equation 2.

$$PSNR = 20\log_{10}(255/\ MSE)\ dB \qquad (2)$$

III *Capacity*: It is the size of the data in a cover image that can be modified without deteriorating the integrity of the cover image. The steganographic embedding operation needs to preserve the statistical properties of the cover image in addition to its perceptual quality. The percentage of Hiding Capacity is given in Equation 3.

$$\text{Hiding Capacity} = (P_{ij} / C_{ij}) * 100 \qquad (3)$$

Where, Pij is the payload image dimensions,

Cij is the cover image dimensions.

3.2 Proposed Embedding Model

In the proposed method, the concept of Dual Tree Complex Wavelet Transform is used to transform the cover image into low and high frequency sub bands. The payload is transformed into frequency domain using lifting wavelet transformation. The approximation band coefficients of payload are embedded into coefficients of high frequency sub bands of cover image to generate stego image based on the entropy of cover image and scaling factor. The block diagram of the proposed embedding model is as shown in Figure 1.

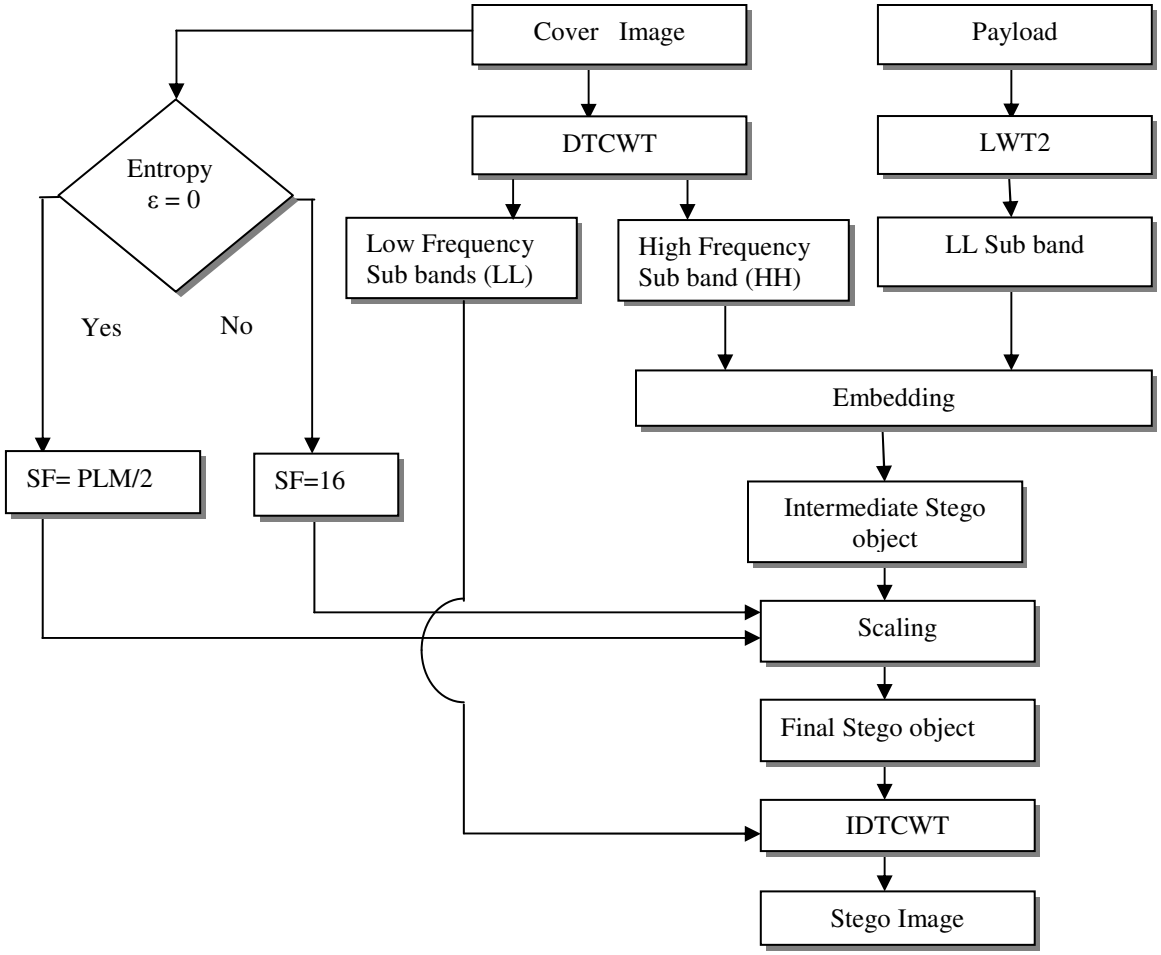

FIGURE 1: Embedding Model of Proposed Algorithm.

3.2.1 Cover image (CI): The cover image of any size and format is considered to test the performance analysis. The cover image is resized to a square matrix dimensions to embed payload for better performance.

3.2.2 Payload: The secret image to be transmitted is embedded into cover image to generate a stego image. The payload may be of any format and of size less than or equal to cover image.

3.2.3 Lifted Wavelet Transform 2 [24]: The main feature of the lifting scheme is that all constructions are derived in the spatial domain. It does not require complex mathematical calculations that are required in traditional methods. Lifting scheme is simplest and efficient algorithm to calculate wavelet transforms. It does not depend on Fourier transforms. Lifting scheme is used to generate second-generation wavelets, which are not necessarily translation and dilation of one particular function. The lifting scheme of wavelet transform has the following advantages over conventional wavelet transform technique. (i) It allows a faster implementation of the wavelet transform. It requires half number of computations as compare to traditional convolution based discrete wavelet transform. This is very attractive for real time low power applications. (ii) The lifting scheme allows a fully in-place calculation of the wavelet transform. In other words, no auxiliary memory is needed and the original signal can be replaced with its wavelet transform. (iii) Lifting scheme allows us to implement reversible integer wavelet transforms. In conventional scheme it involves floating point operations, which introduces rounding errors due to floating point arithmetic.

Constructing wavelets using lifting scheme consists of (i) Split phase (ii) Predict phase (iii) update phase as shown in Figure 2

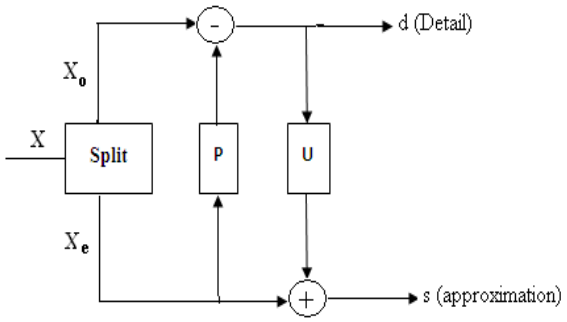

FIGURE 2: Lifting Scheme Implementation.

The first step in the lifting scheme is to separate the original sequence (X) into two sub sequences containing odd indexed samples and even indexed samples. This sub sampling is called as lazy wavelet transform

$$X_o : d_i \leftarrow X_{2i+1}$$

$$X_e : s_i \leftarrow X_{2i}$$

The prediction phase is also called dual lifting (P). This is performed on the two sequences Xo and Xe which are highly correlated. Hence, the predictor P can be used to predict one set from the other. In this step the odd sample are predicted using the neighboring even indexed samples and the prediction error is recorded replacing the original sample value, thus providing in- place calculations.

$$d_i \leftarrow d_i - P(S_A)$$

Where, $A = (i - [N/2] + 1, \ldots\ldots\ldots\ldots\ldots\ldots i + [N/2])$

N = number of vanishing moments in d. this sets the smoothness of the P function.

Update phase is the second lifting step also called as primal lifting (U). Here the even samples are replaced with smoothed values using update operator (U) on previously computed details. The U operator is designed to maintain the correct running average of the original sequence, to avoid aliasing.

$$S_i \leftarrow S_i + U(d_B)$$

Where, $B = \left(i - \left\lfloor \hat{N}/L \right\rfloor, \ldots\ldots\ldots i + \left\lceil \hat{N}/L \right\rceil - 1\right)$

$\hat{N}$ is the number of real vanishing moments

The U operator preserves the first $\hat{N}$ moments in the S sequence, The lazy wavelet is lifted to a transform with required properties by applying dual and primal lifting pair of operations one or more times. Finally, the output streams are normalized using the normalizing factor K.

$$d_i \leftarrow d_i - {}^{1}/_{k}\, s_i \leftarrow s_i * k$$

The output from the S channel after the dual lifting step provides a low pass filtered version of the input, where as the output from the d channel after the dual lifting steps provide the high pass filtered version of the input. The inverse transform is obtained by reversing the order and sign of the operations performed in the forward transform.

The LWT 2 is applied on resized Payload to transform from spatial domain to wavelet domain bands such as Approximation band (LL), Horizontal band (LH), Vertical band (HL) and Diagonal band (HH). The LL band has significant information hence coefficients of LL band is embedded into high frequency sub bands of cover image.

3.2.4 Dual Tree Complex Wavelet Transform [25]: A recent enhancement to DWT with additional, directionality properties. It is an effective approach for implementing an analytic wavelet transform. This is nearly shift invariant and directionally selective in two and higher dimensions this is achieved with a redundancy factor of only 2^d for d-dimensional signals, which is comparatively lower than the undecimated DWT. The idea behind dual tree approach is that it employs two real DWT in its structure. The first DWT gives the real part of the transform and second part gives the imaginary part. The two real wavelet transforms use two different sets of filters, with each satisfying the perfect reconstruction conditions. The two sets of filters are jointly designed so that the overall transform is approximately analytic. The analysis Filter banks used in DTCWT are shown in Figure 3.

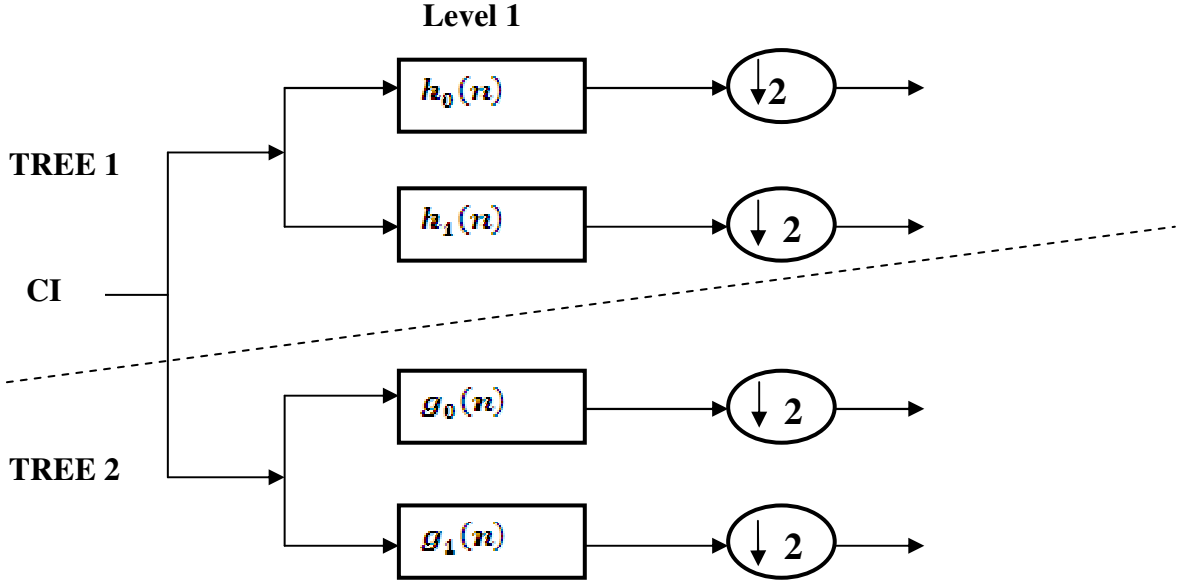

FIGURE 3: Analysis filter bank structure of DTCWT.

Let $h_0(n)$, $h_1(n)$ denote the low-pass and high-pass filter pair for the upper filter bank that is filter bank of tree 1, and let $g_0(n)$, $g_1(n)$ denote the low-pass and high-pass filter pair for the lower Filter Bank that is filter bank of tree 2. The two real wavelets associated with each of the two real wavelet transforms are denoted as $\psi_h(t)$ and $\psi_g(t)$. In addition to satisfying the perfect reconstruction conditions, the filters are designed so that the complex wavelet shown in Equation 4 is approximately analytic.

$$\psi(t) = \psi_h(t) + j\,\psi_g(t) \quad (4)$$

Equivalently, they are designed so that $\psi_g(t)$ is approximately the Hilbert transform of $\psi_h(t)$ as shown in Equation 5.

$$\psi_g(t) \approx \mathcal{H}\{\psi_h(t)\} \quad (5)$$

The implementation of the DTCWT does not require complex arithmetic because filters are themselves real. DTCWT is not a critically sampled transform; it is two times expansive in 1-D because the total output data rate is exactly twice the input data rate. The dual tree CWT is also easy to implement because there is no data flow between the two real DWTs, the transform is naturally parallelized for efficient implementation however, the dual tree CWT requires the design of new filters. Primarily, it requires a pair of filter sets chosen so that the corresponding wavelets form an approximate Hilbert transform pair. Existing filters for wavelet transforms should not be used to implement both the trees of the dual tree CWT. If the dual tree wavelet transform is implemented with filters not satisfying this requirement, then the transform will not provide the full advantages of analytic wavelets.

In the proposed technique a single level of DTCWT is applied to the cover image which gives 12 high frequency sub-bands and 4 low frequency sub bands, only the high frequency sub bands which forms the real part is suitable for embedding as it gives good retrieval quality of the payload without any perceptive degradation to the stego image. In the proposed technique one of high frequency sub band with negligible randomness is selected for embedding. Referring to the Figure 3 the formation of sub-bands in DTCWT can be analyzed as follows (i) The use of filters of Tree 1 alone in both the dimensions that is along rows and columns gives four sub-bands namely LL, LH, HL and HH (ii) The use of filters of Tree 1 along the rows and Tree 2 filters along the columns produces another set of four sub-bands namely LL, HL, LH and HH. (iii) In another combination the filters of Tree 2 are used along the rows and the filters of Tree1 are used along the column to produce yet another set of sub bands namely LL, HL, LH and HH. (iv) finally, the use of Filters of Tree 2 alone in both the dimensions that is along rows and columns produces another set of sub-bands LL, HL, LH and HH.

Thus, a single level of DTCWT when applied to the cover image gives totally 16 frequency sub-bands out of which 4 are LL bands and 12 high frequency sub-bands.

3.2.5 Embedding: The new concept of embedding is used in the proposed model. Here, the chosen high frequency sub band coefficient of the transformed cover image is completely replaced by the LL band coefficient of the payload image. Since coefficients of high frequency sub band of the image are replaced it does not result in the perceptive degradation of the stego image. The use of coefficient replacement method of embedding also gives good retrieval quality of the payload at the receiver end.

3.2.6 Scaling: Scaling operation at the sender end is performed by dividing all the coefficients of the intermediate stego object by a scaling factor. Since the LL sub band coefficients of payload completely replaces the high frequency sub band coefficients of the cover image, only two HH sub bands from real part of DTCWT are used for embedding to get better stego image quality and

also to get perceptively good extracted payload at the destination. The coefficients of two HH sub bands are totally replaced by LL sub band coefficients of payload to generate final stego object. scaling has to be performed to restore the regular pattern of the DTCWT coefficients so that all the high frequency coefficients will have smaller values their by giving fewer chances for suspicion. If only the band in which embedding is done is scaled then only that particular band will show a different pattern of coefficients hence all the high frequency sub bands are scaled so that all of them look almost similar thereby avoiding suspicion. The scaling also improves the security of the payload in the stego image.

3.2.7 Entropy: Entropy [26] is a statistical measure of randomness that can be used to characterize the texture of the image. An image X of size M*N can be considered as a system with 'L' pixel intensity scales. For example, a 8-bit gray image allows L = 256 gray scales from 0 to 255. The probability of i^{th} pixel is given by Equation 6.

$$P_i = \Pr(X = l) = \frac{N(l)}{MN} \quad (6)$$

Where, X = image of size M*N

l= intensity levels varies from 0 to 255 for gray scale image
N(*l*)= No. of pixels with intensity values *l*

Then the entropy of an image is given by Equation 7

$$H(X) = -\sum_{l=0}^{255} P_l \log_2 P_l = \sum_{l=0}^{255} \frac{N(l)}{MN} \log_2 \frac{MN}{N(l)} \quad (7)$$

The image entropy is a quantitative measurement of $\{P_l\}$ where l *v*aries from 0 to 255. It is equivalent to the histogram analysis, which plots the distribution of P_l and is commonly used for security analysis

3.2.8 Scaling Factor: the scaling factor is chosen based on the entropy of cover image.

Case (i): When the Entropy of Cover Image ε =0

When the entropy of cover image is zero the scaling factor is chosen to be half the mean value of payload pixel intensity**.** When this Scaling Factor is used the technique gives good PSNR along with good zero it implies that the randomness of CI is zero hence a high scaling factor can be used as shown in Equation 8

$$SF = \frac{PLN}{2} \quad (8)$$

When Scaling Factor is high the Euclidean distance between the Cover image and stego image is small that is both the images are nearly similar thus giving perceptively good retrieved payload.

Case (ii): When the Entropy of Cover Image ε ≠ 0 in this case when the cover image has randomness a different scaling factor has to be chosen as the stego image will also have randomness. The scaling factor is decided based on the observations by trial and error method where the technique is checked with different formats of image for different scaling factors. It is observed that the scaling factor is independent of the cover image format used hence the same scaling factor can be used for all the formats of cover image. From Table 1 it can be observed that choosing smaller scaling factors in the range 2-10 gives poor stego quality, lesser PSNR but good payload retrieval because the Euclidean Distance (ED) between the intermediate stego object bands before and after transmission is very large. While, Scaling Factor above 15 gives good PSNR, stego quality and retrieval quality but as scaling factor increases the perceptive quality of the retrieved payload becomes poor hence as a trade off to obtain good stego image with good PSNR and good quality of retrieved payload the scaling factor in this case is fixed at

16. Also the histogram pattern of cover image and Stego image are checked for different scaling factors and it is observed that for the scaling factor fixed there is no significant variation in the histogram pattern but smaller scaling factors show significant difference in the pattern

Table 1: Scaling Factor Selection.

Scaling Factor	PSNR(dB)	PSNR1(dB)	ED	Observations
[2-10]	Decreases <30 dB	Increases >40 dB	Higher	Stego Quality- Poor Retrieval Quality- good PSNR- Low Histogram-significant
15	37.3831	32.0704	403.563	Stego Quality – good Retrieval Quality- good PSNR- Good Histogram- insignificant
16	39.3631	36.1902	300.265	
[32 and above]	Increases >40 dB	Decreases <30 dB	Lesser	Stego Quality – good Retrieval Quality- Poor PSNR- Good Histogram-insignificant

Hence the scaling factors used for the proposed techniques are chosen based on the entropy of cover image. Scaling Factor (SF) summarized as shown in Equation 9.

$$SF = \begin{cases} \frac{PLM}{2} = Key1 & \text{if } \varepsilon = 0 \\ 16 = key2 & \text{if } \varepsilon \neq 0 \end{cases} \quad (9)$$

3.2.9 Key: the scaling factor values are used as keys which are embedded in HH sub bands to retrieve payload at the destination**.**

3.2.10 Stego object: The intermediate stego object after performing scaling operation is referred to as stego object. The stego object is the transform domain version of the stego image which will be transmitted through the channel for communication.

3.2.11 Inverse Dual Tree Complex Wavelet Transform (IDTCWT): The inverse of the DTCWT is as simple as the forward transform. To invert the transform, the real part and the imaginary part are each inverted, the inverse of each of the two real DWTs are used, to obtain two real signals. These two real signals are then averaged to obtain the final output. The original signal can also be obtained from either real part or imaginary part alone however, such inverse DTCWTs do not capture all the advantages an analytic wavelet transform offers. IDCTWT is applied on the stego object to generate Stego Image (SI).

3.3 Proposed Extraction Model

In this section the proposed extraction model has been discussed and is shown in Figure 4.

DTCWT is applied on the stego image to extract the high frequency sub bands where the LL sub band of payload embedded in the embedding module. The entropy of stego image is calculated. The scaling factor is fixed at PLM/2 if entropy of stego image is zero else scaling factor is fixed at 16. The coefficients of HH sub band are scaled by multiplying appropriate scaling factors based on entropy of stego image to obtain payload coefficients in wavelet domain. The ILWT2 is applied on payload coefficients to obtain the payload in spatial domain.

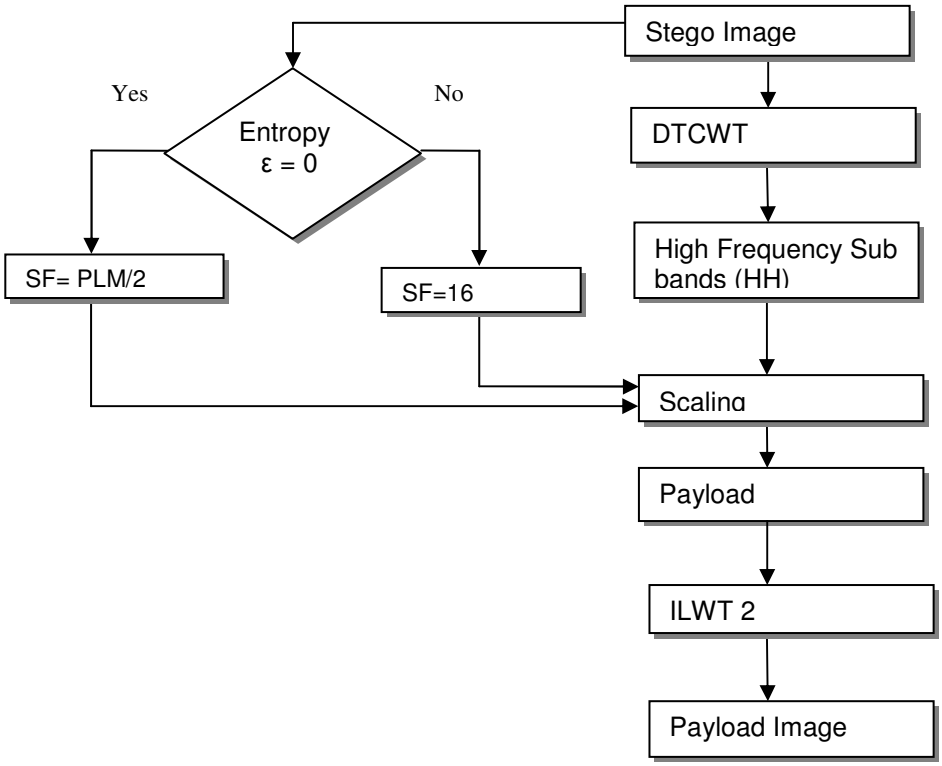

FIGURE 4: Block Diagram of the proposed retrieval model.

4. ALGORITHM

Problem definition: The secret image is embedded into cover image in transform domain using DTCWT technique. In the proposed approach, the new concept to generate stego image is used by replacing the high frequency sub band coefficients of cover image by the approximation band coefficients of the payload.

Assumptions:

(i) The cover and payload objects are gray scale images with different dimensions.
(ii) The stego image is transmitted over an ideal channel.

TABLE 2: Embedding Algorithm of Proposed Model.

Input: Cover image, payload,
Output: Stego image

1. Cover image and Payload image of different formats and sizes are considered
2. Resize CI to $2^m x 2^m$ to apply DTCWT, where m is an integer.
3. Apply one Level DTCWT on the CI
4. Apply one level LWT2 on Payload image
5. The high frequency sub band coefficients of cover image are replaced by LL sub band coefficients of payload in embedding block to generate a stego object.
6. Entropy of cover image is calculated
7. The scaling factor of PLM/2 is fixed if entropy is zero else scaling factor is fixed at 16.
8. The coefficients of intermediate stego object are divided by the appropriate values of scaling factor.
9. The final stego object is generated by scaled intermediate stego object and low frequency sub bands of cover image.
10. Stego image in spatial domain is obtained by applying IDTCWT on the final stego object.

The algorithm of embedding model is discussed in Table 2. The DTCWT and LWT2 are applied on cover image and payload image respectively. The high frequency coefficients of cover image are replaced by LL sub band coefficients of payload. The retrieving algorithm is described in Table 3 to extract payload from stego image by adapting reverse process of embedding.

TABLE 3: Retrieving Algorithm.

Input: Stego image Output: Payload 1. Apply single level DTCWT on the stego image to obtain higher frequency HH sub bands. 2. Entropy of Stego image is computed to fix scaling factor. 3. Scaling factor is PLM/2 if entropy is zero otherwise scaling factor is 16. 4. The high frequency sub band coefficients of DTCWT are multiplied by appropriate scaling factor values to generate payload coefficients. 5. The ILWT2 is applied on payload coefficients to generate payload image in spatial domain.

5. PERFORMANCE ANALYSIS

(i) Histogram Comparison: The payload image Lena.Jpg of size 512 x 512 is embedded into the cover image mandril.Jpg of size 512 x 512 to generate stego image is shown in the Figure 5 using proposed steganographic algorithm.

(a) Cover image (b) Payload (c) *Stego Image* (d) *Retrieved payload*

FIGURE 5: (a) CI: Mandril (512*512) (b) PL: Lena (512*512) (c) Stego Image (512*512) (d) Retrieved payload (512*512).

The histograms of cover image and stego image are shown in Figure 6 the patterns of cover image and stego image histograms are almost same which indicates the statistical properties of stego image are not varied compare to original cover image

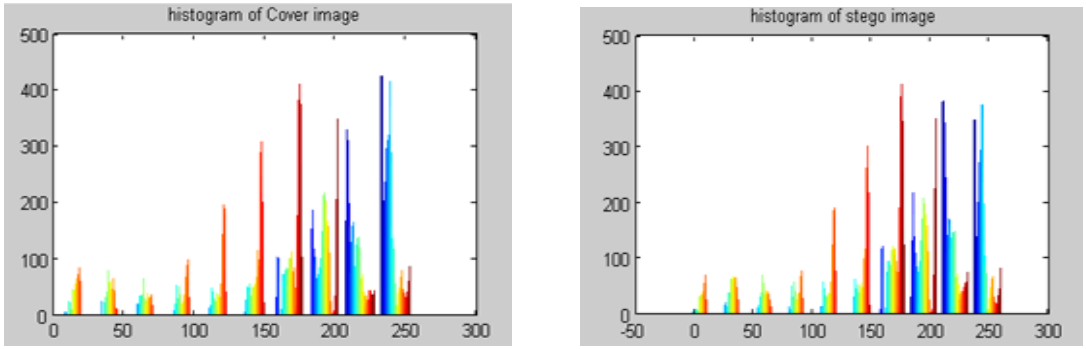

a) Cover image b) Stego image

FIGURE 6: (a) Histogram of CI (b) Histogram of SI.

(ii) Performance Parameters of Proposed Algorithm for different image formats and hiding capacity

The different cover and payload images used to test performance of the proposed algorithm are shown in Figure 7.

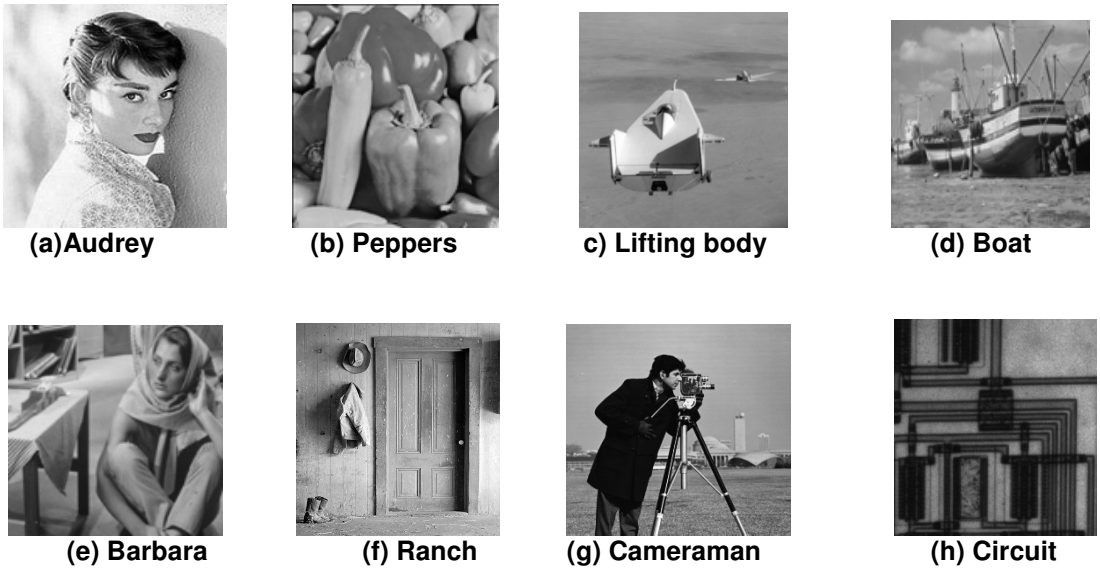

FIGURE 7: Images used as cover and payload with different formats

TABLE 4: Performance Parameters for Different Image Formats With 100% Hiding Capacity.

Cover image (512*512)	Payload (512*512)	(PSNR(CI& SI))	(PSNR(PL&EPL))	Entropy (CI)	Entropy (SI)
Mandril.jpg	lena.tif	42.9421	36.9712	0	0
	audrey.Jpg	42.9096	37.2117	0	0
	ranch.bmp	42.9505	35.3612	0	0
	liftingbody.Png	43.0296	37.4578	0	0
Audrey.jpg	lena.tif	41.5943	42.2837	0.0058	0.0014
	barbara.jpg	41.6521	38.7104	0.0058	0.00051
	ranch.bmp	41.77	37.2746	0.0058	0
	liftingbody.png	41.724	35.2302	0.0058	0.000518
circuit.tif	lena.tif	39.8503	36.9188	0	0
	barbara.jpg	39.8570	30.8117	0	0
	ranch.bmp	39.8472	35.3104	0	0
	liftingbody.png	39.8809	37.3862	0	0
Mandril.tif	lena.tif	32.3845	29.5074	0.000074	0.00072
	barbara.Jpg	32.4569	29.5074	0.000074	0.00317
	ranch.bmp	32.2646	27.3367	0.000074	0.00074
	liftingbody.png	32.1867	27.2270	0.000074	0.0420
Liftingbody.png	lena.tif	36.7624	37.7115	0.0014	0.0036
	barbara.jpg	35.4529	29.7459	0.0014	0.0018
	pirate.bmp	35.8598	31.4215	0.0014	0.000518
	mandril.png	35.08596	27.5279	0.0014	0.0051

The cover and payload images are converted into transform domain and the payload is embedded into the cover to derive the stego image. The payload is retrieved from stego image using reverse embedding process at the destination. The performance parameters such as PSNR between cover image and stego image PSNR (CI& SI), PSNR between payload & Extracted payload (PSNR (PL&EPL)), entropy of cover image (CI) and entropy of stego image (SI) with hundred percent hiding capacity are tabulated in Table 4. The PSNR between cover and stego image is almost constant irrespective of payload image formats. The value of PSNR between the cover and stego image depends on the cover image format and also entropy of cover image. The PSNR between cover and stego image is little high when the entropy is zero compare to entropy of non zero value, since scaling factor is high in the case of entropy zero compared to lower scaling factor for non zero entropy value. The values of PSNR are high in the case of JPG image format of the cover image compare to Tiff, PNG and Bmp formats of cover image.

The performance parameters such as PSNR between cover image and stego image PSNR (CI& SI), PSNR between payload & Extracted payload PSNR (PL&EPL), entropy of cover image (CI) and entropy of stego image (SI) with seventy five percent hiding capacity are tabulated in Table 5

TABLE 5: Performance Parameters for Different Image Formats With 75% Hiding Capacity.

Cover image (512*512)	**Payload (512*384)**	**PSNR (CI& SI)**	**PSNR(PL&EPL)**	**Entropy (CI)**	**Entropy (SI)**
Mandril.jpg	lena.tif	43.2743	37.1437	0	0
	audrey.Jpg	43.1747	42.3191	0	0
	ranch.bmp	43.3095	35.4160	0	0
	liftingbody.Png	43.3713	37.4115	0	0
Audrey.jpg	lena.tif	41.9756	36.9878	0.0058	0.0042
	barbara.jpg	41.8893	42.3596	0.0058	0.0020
	ranch.bmp	41.9995	35.2554	0.0058	0.0094
	liftingbody.png	42.0413	37.1860	0.0058	0.0034
circuit.tif	lena.tif	40.0347	30.7472	0	0
	barbara.jpg	40.0230	36.8722	0	0
	ranch.bmp	40.0276	35.3737	0	0
	liftingbody.png	40.0523	37.3488	0	0
Mandril.tif	lena.tif	32.7592	33.2747	0.000074	0.0365
	barbara.Jpg	33.2413	37.3500	0.000074	0.0848
	ranch.bmp	33.7029	30.8545	0.000074	0.0235
	liftingbody.png	32.5427	30.2076	0.000074	0.0081
Liftingbody .png	lena.tif	36.0756	30.7044	0.0014	0.0034
	barbara.jpg	37.1842	37.6696	0.0014	0.0049
	pirate.bmp	35.7648	30.5444	0.0014	0.00096
	peppers.png	36.4326	31.4281	0.0014	0.00034

The performance parameters such as PSNR between cover image and stego image PSNR (CI& SI), PSNR between payload & Extracted payload PSNR (PL&EPL), entropy of cover image (CI) and entropy of stego image (SI) with fifty percent hiding capacity are tabulated in Table 6 The performance parameters such as PSNR between cover image and stego image PSNR (CI& SI), PSNR between payload & Extracted payload PSNR (PL&EPL), entropy of cover image (CI) and entropy of stego image (SI) with twenty five percent hiding capacity are tabulated in Table 7

TABLE 6: Performance Parameters for Different Image Formats With 50% Hiding Capacity.

Cover image (512*512)	**Payload (512*256)**	**PSNR(CI& SI)**	**(PSNR(PL&EPL))**	**Entropy (CI)**	**Entropy (SI)**
Mandril.jpg	lena.tif	43.6027	42.1814	0	0
	audrey.Jpg	43.6764	37.0397	0	0
	ranch.bmp	43.7017	35.5876	0	0
	liftingbody.Png	43.7466	37.3530	0	0
Audrey.jpg	lena.tif	42.2057	36.9101	0.0058	0.0071
	barbara.jpg	42.2649	42.0915	0.0058	0.00097
	ranch.bmp	42.2865	35.4492	0.0058	0.0030
	liftingbody.png	42.3165	371642	0.0058	0.0062
circuit.tif	lena.tif	40.2101	36.7554	0	0
	barbara.jpg	40.2019	37.0028	0	0
	ranch.bmp	40.2115	35.5477	0	0
	liftingbody.png	40.2292	37.3008	0	0
Mandril.tif	lena.tif	33.4252	35.4106	0.000074	0.0308
	barbara.Jpg	33.0838	37.0545	0.000074	0.0950
	ranch.bmp	32.9752	30.4197	0.000074	0.0149
	liftingbody.png	33.9277	30.4724	0.000074	0.0018
Liftingbody.png	lena.tif	37.6512	30.6509	0.0014	0.0022
	barbara.jpg	36.8103	37.5773	0.0014	0.0044
	pirate.bmp	36.5643	30.6171	0.0014	0.0014
	mandril.png	37.0894	31.4623	0.0014	0.0021
Ranch.bmp	lena.tif	36.1504	30.4790	0.0005	0.0102
	barbara.jpg	38.2569	37.2016	0.0005	0.0067
	pirate.bmp	36.1139	32.8101	0.0005	0.0171
	liftingbody.png	36.0994	31.2288	0.0005	0.0054

The performance parameters PSNR (CI & SI) and varies between PSNR (PL & EPL) are tabulated in Table 8 for different percentage capacities with cover and payload images having JPG formats. The values of PSNR (CI & SI) are almost constant for percentage hiding capacities between 25 and 100. The variations of PSNR (CI & SI) and percentage hiding capacity are plotted in the Figure 8 as the percentage hiding capacity increases from 25 to 100, the values of

PSNR (CI & SI) varies between 44.43 and 43. 91 ie., the PSNR values are almost constant with capacity.

TABLE 7: PSNR Performance Parameters for Different Image Formats With 25% Hiding Capacity.

Cover image (512*512)	Payload (256*256)	(PSNR(CI& SI))	(PSNR(PL&EPL))	Entropy (CI)	Entropy (SI)
Mandril.jpg	lena.tif	44.4238	45.7815	0	0
	audrey.Jpg	44.4274	41.6053	0	0
	ranch.bmp	44.7086	44.427	0	0
	liftingbody.Png	44.7086	53.6653	0	0
Audrey.jpg	lena.tif	42.7972	44.1040	0.0058	0.0061
	barbara.jpg	42.7962	43.501	0.0058	0.00051
	ranch.bmp	42.7992	43.0021	0.0058	0.0080
	liftingbody.png	42.8008	49.4367	0.0058	0.00047
circuit.tif	lena.tif	40.5275	52.7875	0	0
	barbara.jpg	40.5256	45.4012	0	0
	ranch.bmp	40.5260	44.3152	0	0
	liftingbody.png	40.5282	52.592	0	0
Mandril.tif	lena.tif	38.6174	36.7372	0.000074	0.0012
	barbara.Jpg	36.4341	30.25	0.000074	0.003
	ranch.bmp	37.3432	31.653	0.000074	0.0012
	liftingbody.png	38.4401	30.2705	0.000074	0.0061
Liftingbody.png	lena.tif	37.6172	31.8271	0.0014	0.0013
	barbara.jpg	37.6735	30.5944	0.0014	0.0021
	pirate.bmp	37.5189	30.6333	0.0014	0.0016
	mandril.png	37.8463	31.4820	0.0014	0.0023
Ranch.bmp	lena.tif	37.2856	33.0564	0.0005	0.0061
	barbara.jpg	38.3256	33.5432	0.0005	0.0016
	pirate.bmp	37.4265	32.1544	0.0005	0.0047
	liftingbody.png	38.2330	31.2061	0.0005	0.0062

TABLE 8: Performance Analysis of the Proposed Technique for Different Hiding Capacity.

Cover Image [Mandril.jpg]	Payload Image [Barbara.jpg]	%Capacity	PSNR (CI&SI) (dB)	PSNR(PL&EPL) (dB)
512*512	256*256	25	44.4238	45.7815
512*512	512*256	50	43.9852	37.0397
512*512	512*384	75	43.9543	37.1437
512*512	512*512	100	43.9100	36.9712

iii) Comparison of performance parameters of proposed algorithm with existing algorithms.

Table 9 shows the comparison of PSNR (CI& SI)) and percentage Hiding Capacity (HC) of proposed technique and the existing techniques. The percentage hiding capacities of the proposed algorithm is 100% with PSNR (CI & SI) varies between 35.79 and 42.94 based on cover images are compared with existing techniques presented by Hoda Motamedi and Ayyoob

Jafari [27], Tasnuva Mahajabin et. al., [28] and Ashish Soni et.al.,[29]. It is observed that the PSNR values and percentage hiding capacity values are higher in the case of proposed algorithm compare to existing algorithms for the following reasons.

(i)The percentage hiding capacity is 100% since six high frequency sub bands which form the real are used for embedding payload with good payload retrieval quality at the destination.

(ii) The scaling factor is chosen based on the entropy of the cover image. When the entropy is zero the scaling factor is high, this reduces the Euclidean distance between the high frequency sub bands of cover image and stego image, thus giving high PSNR and good retrieval payload quality.

(iii) The PSNR value does not vary significantly though the capacity is varied because of the high frequency sub bands which have negligible randomness.

(iv) when the entropy of cover image is non zero then the scaling factor is reduced from higher value and fixed at 16 to obtain better quality of retrieved payload image at the destination. The PSNR (CI&SI) is decreased since scaling factor is reduced.

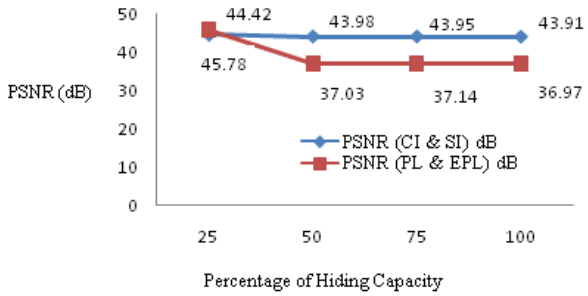

FIGURE 8: variation of PSNR and hiding capacity.

TABLE 9: Comparison of capacity and value of proposed algorithm with the existing algorithms.

Authors	Technique	Cover image	PSNR (CI & SI) (dB)	HC (%)
Hoda Motamedi and Ayyoob Jafari [27]	Wavelet transform and image denoising techniques.	Barbara	39.65	62.37
		Boat	36.34	76.87
Tasnuva Mahajabin et. al.,[28]	Pixel value differencing and LSB substitution Method	Mandril	32.67	47.93
Ashish Soni et.al.,[29]	Discrete Fractional fourier Transform.	Rice	32.46	100
Proposed	coefficient replacement and adaptive scaling steganography based on DTCWT	Barbara	41.05	100
		Boat	42.49	100
		Mandrilla	42.94	100
		Rice	35.79	100

6. CONCLUSIONS

In this paper, an algorithm for embedding DTCWT based LL sub band coefficients of secret information into HH sub band coefficients of cover image using adaptive scaling is proposed. The novel coefficient replacement technique improves the security, PSNR and 100 percent hiding capacity. The adaptive scaling and use of DTCWT transformation yields better results compared to the existing techniques. In future, the proposed technique can be used in spatial domain.

7. REFERENCES

[1] Rig Das and Themirchon Tuithung, "A Novel Steganography Method for Image Processing Based on Huffman Encoding," Third National Conference on Emerging Trends and Applications in Computer Science, pp. 14-18, March 2012.

[2] Najeena K S and B M Imran, "An Efficient Steganographic Technique based on Chaotic Maps and Adpative PPM Embedding," International Conference on Signal Processing, Image Processing & Pattern Recognition, pp. 293 – 297, 2013.

[3] Ran-Zan Wang and Yeh-Shun Chen, "High-Payload Image Steganography using Two-way block Matching," IEEE Signal Processing Letters, Vol. 13, Issue 3, pp. 161 – 164, 2006.

[4] Vojtech Holub and Jessica Fridrich, "Designing Steganographic Distortion using Directional filters," IEEE International Workshop on Information Forensics and Security, pp. 234 – 239, 2012.

[5] BaolongGuo, Leida Li, Jeng-Shyang Pan, Liu Yang and Xiaoyue Wu, "Robust Image Watermarking Using Mean Quantization in DTCWT Domain," Eighth International Conference on Intelligent Systems Design and Applications, pp. 19 – 22, 2008.

[6] Ajit Danti and G R Manjula, "Secured Data Hiding of Invariant Sized Secrete Image based on Discrete and Hybrid Wavelet Transform," IEEE International Conference on Computational Intelligence & Computing Research, pp. 1 – 6, 2012.

[7] L Jani Anbarasi and S.Kannan, "Secured Secret Color Image with Steganography," IEEE International Conference on Recent Trends in Information Technology, pp. 44 - 48, 2012.

[8] V Sathya, K Balasubramaniyam, N Murali, M RajaKumaran and Vigneswari, "Data Hiding in Audio Signal, Video Signal, Text and JPEG Images," International Conference on Advances in Engineering Science and Management, pp. 741-746, 2012.

[9] Zawawi M. N. Mahmood. R, Udzir. N, Ahmad. F and Desa J. M, "Active Warden as the Main Hindrance for Steganography Information Retrieval," IEEE Information Retrieval and Knowledge Management International Conference, pp. 277-280, 2012.

[10] Ching-Nung Yang, Tse- Shih Chen, Kun Hsuan and Chung- Chun Wang, "Improvement of Image Sharing with Steganography and Authentication," Journal of System and Software, Elsevier , Vol 80, issue 7, pp. 1070 - 1076, July 2007.

[11] Chiang- lung Liu and Shiang- Rong Liao, "High Performance JPEG Steganography Using Complementary Embedding Stratergy," Pattern Recognition, Vol. 41, issue 9, Elsevier, pp. 2945-2955, September 2008.

[12] H. S. Manjunatha Reddy and K. B. Raja, "High Capacity and Security Steganography Using Discrete Wavelet Transform," International Journal of Computer Science and Security, vol. 3, issue 6 , pp. 462-472, 2010.

[13] K B ShivaKumar, K B Raja and Sabyasachi Patnaik, "Hybrid Domain LSB Steganography," International Journal of Computer Applications, Vol 19. No.7, pp. 35 - 39, April 2011.

[14] Youngran Park, Hyunho Kang, Kazuhiko Yamaguchi and Kingo Kobayashi, "Intergrity Verification of Secret Information in Image Steganography," The Twenty ninth Symposium on Information Theory and its Applications, pp. 1 – 4, 2006.

[15] Xinpeng Zhang and Shou Zhang Wang, "Vulnerability of Pixel Value Differencing Steganography to Histogram Analysis and Modification for Enhanced Security," Pattern Recognition Letters, vol 25, issue 3, Elsevier, pp.331-339, February 2004.

[16] Chin - Chan Chang and Hsien- Wen Tseng, "A Steganographic Method for Digital Images Using Side," Pattern Recognition Letters, vol 25, issue 12, Elsevier, pp. 1431-1437, September 2004.

[17] H S Manjunatha Reddy and K B Raja, "Wavelet Based Non LSB Steganography," International Journal of Advanced networking and applications, vol 3, issue 3 pp. 1203 – 1209, 2011.

[18] K B Shiva Kumar, K.B. Raja, R. K. Chhotray and Sabyasachi. Patnaik, "Bit Length Replacement Steganography Based on DCT Coefficients," International Journal of Engineering Science and Technology, vol. 2(8), pp. 3561-3570, 2010.

[19] K B Shiva Kumar, K B Raja, R K Chhotray and Sabyasachi Patnaik, "Steganography Based on Payload Transformation," International Journal of Computer Science Issues, vol 8, Issue 2, pp. 241-246, March 2011.

[20] H S Manjunatha Reddy and K B Raja, "Wavelet Based Secure Steganography With Scrambled Payload," International Journal of Innovative Technology and Exploring Engineering, vol. 1, issue 2, pp.121 - 129, July 2012.

[21] Arnab Kumar Maji, Rajkumar Pal and Sudipta Roy, "A Novel Steganographic Scheme using Sudoku," International Conference on Electrical Information and Communication Technology (EICT), 2013 pp. 1 – 6, 2013.

[22] Md. Rashedul Islam, Ayasha Siddiqa, Md. Palash Uddin, Ashis Kumar and Md. Delowar Hossain, "An Efficient Filtering based Approach Improving LSB Image Steganography using Status Bit along with AES Cryptography," Third IEEE International Conference on Informatics, Electronics and Vision, pp. 1-6, 2014.

[23] Chi Yuan Lin, Shu cing Wu and Jyuan Jie Wang, "VQ Image Compression Steganography based on Section based Informed Embedding," International Symposium on Computer, Consumer and Control, pp. 111 – 114, 2014.

[24] W Sweldens, "The Lifting Scheme: A Construction of Second Generation Wavelets," SIAM Journal in Math. Analysis, vol. 29, no. 2, pp.511 – 546, 1998.

[25] Ivan.W.Selesnick, Richard.G.Baraniuk and Nick G. Kingsbury, "The Dual-Tree Complex Wavelet Transform," Signal Processing Magazine IEEE, Vol. 22, issue 6, pp. 123-151, 2005.

[26] Yue Wu, Joseph P Noonan and SOS Agaian, "Shannon Entropy based Randomness Measurement and Test for Image Encryption," Journal of Information sciences, Elsevier, pp. 1 – 23, 2011.

[27] Hoda Motamedi and Ayyoob Jafari, "A New Image Steganography based on Denoising Methods in Wavelet Domain," Ninth International Conference on Information Security and Cryptology, pp. 18 – 25, 2012.

[28] Tasnuva Mahjabin, Syed Monowar Hossain, and Md. Shariful Haque, “A Block Based Data Hiding Method in Images using Pixel Value Differencing and LSB Substitution Method,” Fifteenth International Conference on Computers and Information Technology, pp. 168 – 172. 2012.

[29] Ashish Soni, Jitendra jain and Rakesh Roshan, “Image Steganography using Discrete Fractional Fourier Transform,” International Conference on Intelligent Systems and Signal Processing, pp. 97 – 100. 2013.

Realtime Energy Efficient Digital Image Watermarking on Mobile Devices using Android

Durgansh Sharma *durgansh.sharma@jaipuria.ac.in*
Ph.D. Student, UPES, Dehradun India
Asst. Professor, Jaipuria Institute of Management, Noida, India

Manish Prateek *mprateek@ddn.upes.ac.in*
Professor, Centre For Information Technology,
College of Engineering Studies, UPES, Dehradun, India

Tanushyam Chattopadhyay *t.chattopadhyay@tcs.com*
Senior Scientist, R&D, Innovation Lab,
Tata Consultancy Services, Kolkata, India

Abstract

This paper proposes a real time and energy efficient image watermarking scheme using DCT – DWT hybrid transformation. The proposed method is using a 2 – level of quantization on the Y component of true color image captured in real time and low frequency band coefficients are selected for the dataset prepared of size 256 * 10 using these coefficients, which is supplied to Extreme Learning Machine (ELM) a single layer feed forward network. A normalized column vector of size 256 * 1 is generated by ELM for its usage as key sequence for embedding the watermark. This hybrid transforms provide a better imperceptibility and reduction in the time taken by entire watermarking process i.e. within a second, makes it energy efficient and suitable for the proposed smart phone android app for a real time image watermarking.

Keywords: Real Time, Smart Phone, Android, Image Watermarking, Extreme Learning Machine (ELM), Discrete Cosine Transform (DCT), Discrete Wavelet Transform (DWT).

1. INTRODUCTION

Exponential rise in generation and sharing of digital images using smart phones has created an influx of multimedia data, which needs to be processed, stored, and transmitted on battery operated mobile devices. Rights and validation of this data has been a major challenge, where mobile devices with converged multimedia features, content authorization and ownership of an image has raised an issue of immense concern in this era of data explosion, for which the authors propose a real time and energy efficient digital watermarking technique to embed and extract watermark for digital images using the android based mobile platform. Growth of mobile phones and wearable mobile devices has outnumbered the growth pattern of laptop and desktop PCs. They are growing on a fast pace, and providing infinite data streams to deal with. Current mobile devices are the perfect example of convergence of all features required for any ICT application. Mostly, the data captured and shared using social media is in the form of photos and images. The problem was to create energy efficient image watermarking technique for mobile phone with various resource constraints mainly battery and time to execute for an application. Proposed model shows fast and energy efficient technique for watermark embedding and extraction from images, thus, signifying a great potential in designing futuristic intelligent mobile devices.

2. REVIEW

Immense research work has been done in the field of image watermarking. The authors found an interesting and upcoming research work done by Miao, N. et al.[16] by creating an android based app 'hymnmark' for offline image watermarking. It has supported while extending the work for real time image watermarking, which needs a technique of fast processing for the same, the research work by Mishra, A. et al.[3] for hybrid transform using DCT-DWT including ELM for a fast algorithm has raised the scope of its usage in mobile devices. Another research work by Sharma, D. et al. [2] which has used fuzzy logic to incorporate HVS while image watermarking in gray scale images with an updated algorithm was designed to work upon color images in the realtime using Simulink and webcam Sharma, D. et al.[1] its real time watermarking is further enhanced and applied in the proposed paper.

Research work proposed by Madhesiya, S. et al.[4], Rajab, L. et al.[8] and Liu, R. et al.[12] showcased other efficient way of factorization used in the watermarking techniques through singular value decomposition (SVD), Rajab, L. et al.[8] has also provided the scope of color image watermarking by performing the video watermarking using SVD. Ramamurthy, N. et al.[5] and Isac B. et al.[6] enhanced the techniques of image and video watermarking using Fuzzy Logic and Neural networks. Lin, T. C. et al.[7] has given an insight regarding wavelet based copyright protection for images. Huang, G. B., et al.[10,11] has provided the way of fast learning using Single Layer Feed forward Network (SLFN) commonly known as Extreme Learning Machine, it has become the most useful means for this study as realtime learning on a mobile phone platform is essentially needed to be fast.

The concept hidden image copyright labeling provided by Koch, E. et al.[13] is used by the author in this research work of real time image watermarking using the most important concept of Kejariwal, A. et al.[9] has provided the concept of energy efficient image watermarking using mobile devices and Miao, N. et al.[16] showcased the runtime watermarking technique using Android platform in the mobile devices.

Discrete Cosine Transformation (DCT) and Discrete Wavelet Transformation (DWT) [2,3,4] are used for image transformation from spatial domain to the frequency domain where signal processing for the watermarking process could be done on host image. Extreme Learning Machine (ELM) [3] is designed with a Single hidden Layer Feed forward Network (SLFN) architecture. The results acquired by using ELM are having a good accuracy and computationally extremely fast as compared with Back Propagation (BP) based algorithms. Android [21] is an open-source software stack for a wide range of mobile devices and a open-source project led by Google. Digital image watermarking is a technique to embed any information in an image to prove confidentiality and ownership in a covert manner. It aims for imperceptibility and robustness as a part of its process.

3. MODELING & ANALYSIS

In continuation to the work done by author, the next step comes out to be incorporation and implementation of the proposed model [1]. Initially, android based mobile "LG Optimus P970" was narrowed down to be used as the hardware component because of its good camera handling capabilities. The camera App namely CameraPHD labeled as "Next Gen Cam!" was initially designed for the purpose of real time image watermarking for Android Froyo (2.2) available in the hardware device, then upgraded to Android Gingerbread (2.3) and finally to Ice Cream Sandwich (4.0).

The image captured by the camera aperture of any android mobile phone through the "Next Gen Cam!" will be processed through the algorithm designed by author for real time energy efficient image watermarking. In this work Koch's algorithm [13] is used as a base for the workflow design due to low power consumption and small execution time which further supports in real time performance of the proposed work.

Embedding process comprises of the Host image captured in real time, information needed to embed as watermark and key for the positioning of watermark. The captured host image is loaded for color space transformation into YUV instead of RGB, as Y component is used for the embedding digital watermark. The proposed method is using DWT for 2 – level of quantization on the Y component of true color image converted from the RGB image captured in real time.

Equation 1: RGB to YUV Conversion

$$\begin{bmatrix} Y' \\ U \\ V \end{bmatrix} = \begin{bmatrix} 0.299 & 0.587 & 0.114 \\ -0.14713 & -0.28886 & 0.436 \\ 0.615 & -0.51499 & -0.10001 \end{bmatrix} \begin{bmatrix} R \\ G \\ B \end{bmatrix}$$

Flow Chart for Watermark Embedding

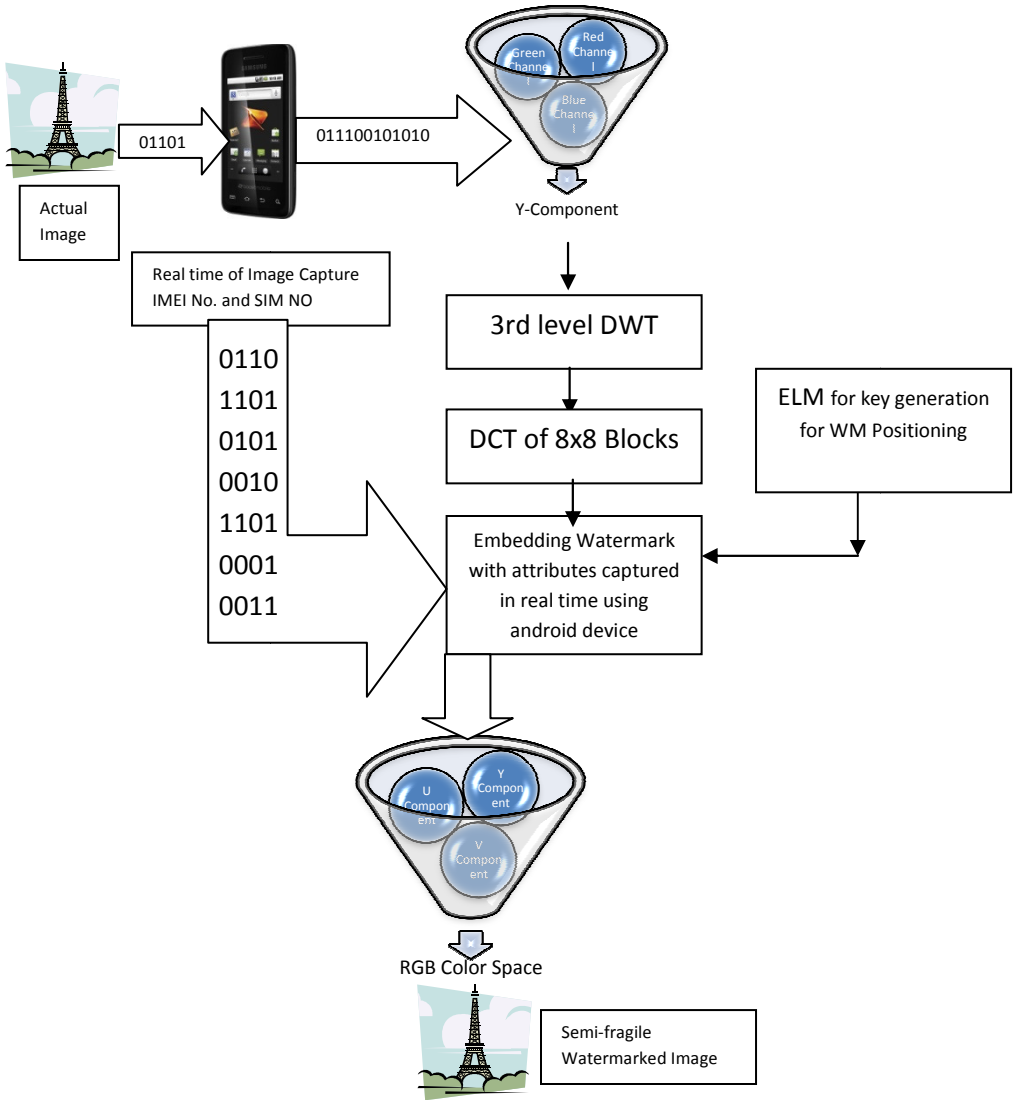

FIGURE 1: Watermark Embedding.

Its low frequency band coefficients are selected for the dataset prepared by DCT of 8x8 blocks integrating to the size 256 * 10 using these coefficients, which is supplied to Extreme Learning

Machine (ELM) a single layer feed forward network. The ELM produces a normalized column vector of size 256 * 1 to be used as key sequence for embedding the watermark consisting of attributes like time of capturing the image, IMEI No. of mobile device, SIM No. of the first carrier captured in real time using the camera app installed in any android mobile device. Further, once the watermarked image is created after embedding process, it leads towards de-quantization and inverse DCT (IDCT) of every block. It is needed to multiplex the embedded blocks to create the Y-component layer and loaded for color space transformation from YUV to RGB to get watermarked image.

Equation 2: YUV to RGB Conversion

$$\begin{bmatrix} R \\ G \\ B \end{bmatrix} = \begin{bmatrix} 1 & 0 & 1.13983 \\ 1 & -0.39465 & -0.58060 \\ 1 & 2.03211 & 0 \end{bmatrix} \begin{bmatrix} Y' \\ U \\ V \end{bmatrix}$$

Flow Chart for Watermark Extraction

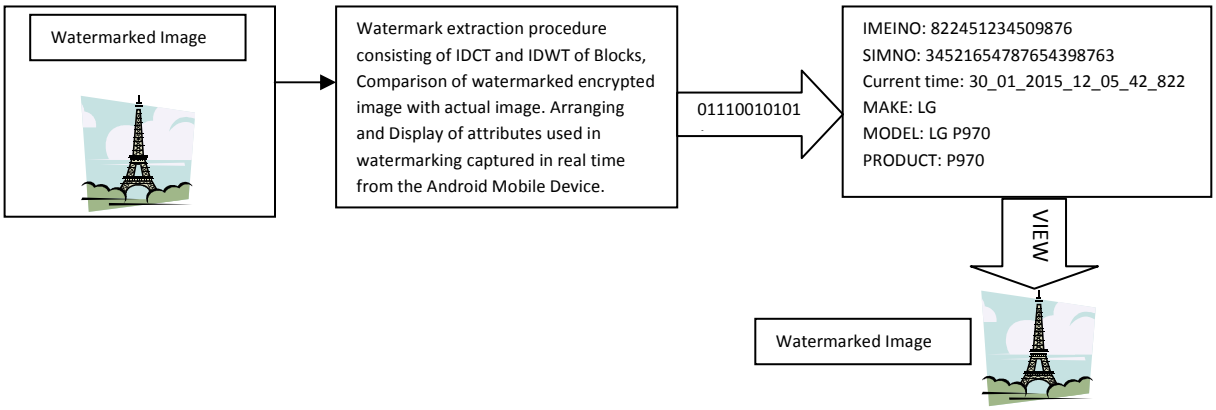

FIGURE 2: Watermark Extraction.

4. RESULTS

Analysis of Time complexity and Energy Efficiency and steps used in image watermarking using Camera App designed by the author are mentioned as following steps:

Initialization: Landing Interface or Layout of Camera App (Fig. 3).

Step 1: Screen after clicking Retrieve Information (Fig. 4)
Step 2: This Screen is shown after clicking File Explorer to showcase the path of image saved. (Fig. 5)
Step 3: If you click Original Image for Retrieval, you won't find any watermark and above information screen will be showcased. (Fig. 6)
Step 4: If encrypted image is clicked for retrieving watermark, you find above information screen showcasing the watermark embedded in the image. (Fig. 7)
Step 5: Once you click "View" you will be able to see the watermarked image. (Fig. 8)
"Original Image" (Fig. 9), Watermarked Image (Fig. 10) for the following energy consumption results by the camera app. Storage path for saving captured and watermarked images. 4th Col, 2nd Row indicates the name of folder "durgansh camera" (Fig. 11).

Results for Energy Consumption calculated by Android App for Real-time system and application power monitor "PowerTutor" referred from [16].

- Overall Energy Consumption by CameraPHD is **34.4 J** (Fig. 12)
- Energy Consumption by CameraPHD for for LCD usage is **31.5 J** (Fig. 13)

- Energy Consumption by CameraPHD for CPU usage is **2.9 J** (Fig. 14)

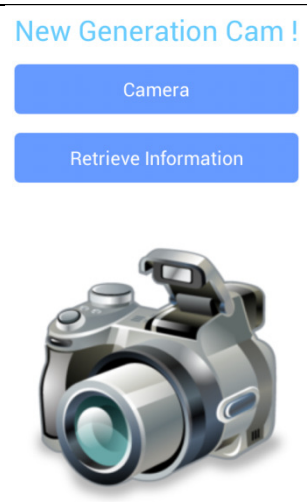

Figure 3: Landing Layout

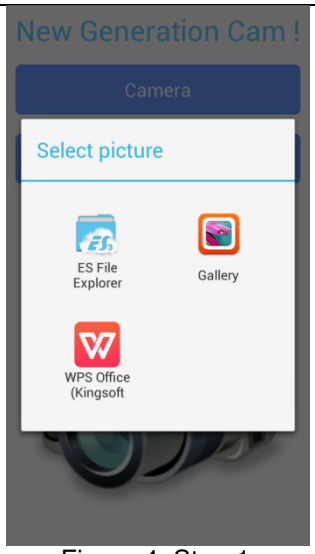

Figure 4: Step 1

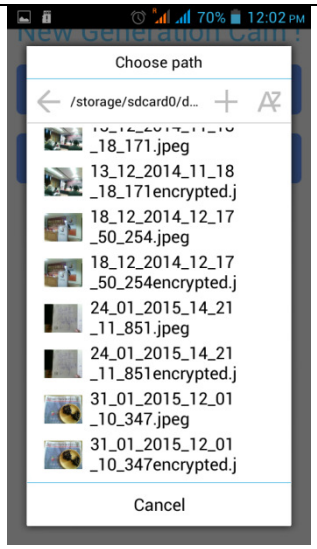

Figure 5: Step 2

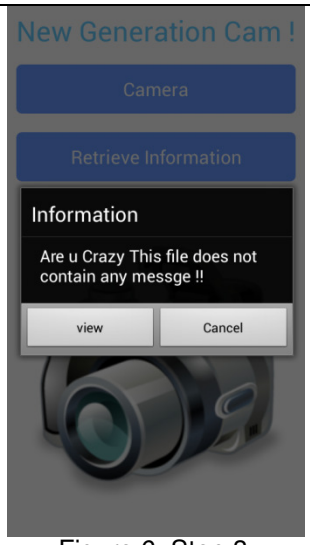

Figure 6: Step 3

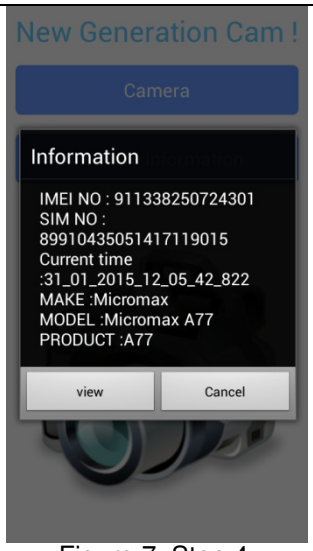

Figure 7: Step 4

Figure 8: Step 5

Figure 9: Original Image

Figure 10: Watermarked Image

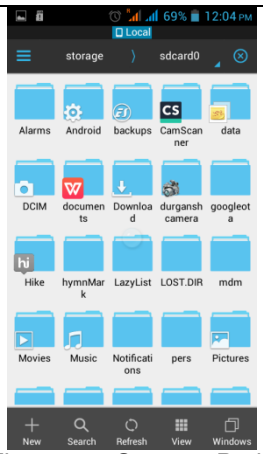

Figure 11: Storage Path

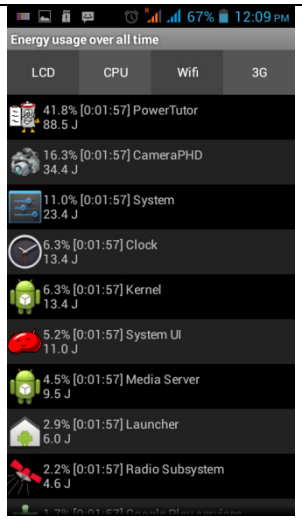

Figure 12: Overall Energy Consumption by Camera App

Figure 13: Energy Consumption by LCD for Camera App

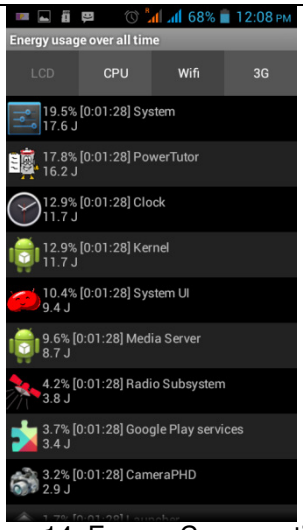

Figure 14: Energy Consumption by CPU for Camera App

5. CONCLUSION

The camera App is successfully tested and working in Android Jelly Bean 4.2.2 providing energy efficient and realtime image watermarking of the ownership credentials which can be extracted using the application installed.

6. FUTURE SCOPE

This research work of energy efficient and real time image watermarking in mobile devices could be further enhanced for various upcoming versions of Android and Models of next generation camera enabled android devices. Extraction of the image watermark could be made generic where essential credentials once provided through cloud services can extract the necessary information from the encrypted image for proving the ownership of the image. This research work could be used in various other camera oriented applications.

7. REFERENCES

[1] Sharma, D., Prateek, M., & Chattopadhyay, T. (2014). DCT and Simulink Based Realtime Robust Image Watermarking. International Journal of Image Processing (IJIP), 8(4), 214-219.

[2] Sharma, D., Prateek, M., & Chattopadhyay, T. (2014). DCT Based Fuzzy Image Watermarking. Global Journal of Enterprise Information System (GJEIS), 6(2), 90-95.

[3] Mishra, A., & Goel, A. (2014). A Novel Image Watermarking Scheme using Hybrid DWT-DCT-ELM Technique. International Journal of Computer Applications, 98(18), 28-33.

[4] Madhesiya, S., & Ahmed, S. (2013). Advanced Technique of Digital Watermarking based on SVD-DWT-DCT and Arnold Transform. International Journal of Advanced Research in Computer Engineering & Technology (IJARCET), 2(5), pp-1918.

[5] Ramamurthy, N., & Varadarajan, D. S. (2012). Robust Digital Image Watermarking Scheme with Neural Network and Fuzzy Logic Approach.International Journal of Emerging Technology, Advanced Engineering, 2(9).

[6] Isac, B., & Santhi, V. (2011). A study on digital image and video watermarking schemes using neural networks. International Journal of Computer Applications, 12(9), 1-6.

[7] Lin, T. C., & Lin, C. M. (2009). Wavelet-based copyright-protection scheme for digital images based on local features. Information Sciences, 179(19), 3349-3358.

[8] Rajab, L., Al-Khatib, T., & Al-Haj, A. (2009). Video watermarking algorithms using the SVD transform. European Journal of Scientific Research, 30(3), 389-401.

[9] Kejariwal, A., Gupta, S., Nicolau, A., Dutt, N. D., & Gupta, R. (2006). Energy efficient watermarking on mobile devices using proxy-based partitioning. Very Large Scale Integration (VLSI) Systems, IEEE Transactions on, 14(6), 625-636.

[10] Huang, G. B., Zhu, Q. Y., & Siew, C. K. (2006). Extreme learning machine: theory and applications. Neurocomputing, 70(1), 489-501.

[11] Huang, G. B., Zhu, Q. Y., & Siew, C. K. (2006). Real-time learning capability of neural networks. Neural Networks, IEEE Transactions on, 17(4), 863-878.

[12] Liu, R., & Tan, T. (2002). An SVD-based watermarking scheme for protecting rightful ownership. Multimedia, IEEE Transactions on, 4(1), 121-128.

[13] Koch, E., & Zhao, J. (1995, June). Towards robust and hidden image copyright labeling. In IEEE Workshop on Nonlinear Signal and Image Processing (pp. 452-455). Neos Marmaras, Greece.

[14] D. Sharma, M. Prateek, T. Chattopadhyay, “Optimized Robust Image Watermarking”, Proceedings of 4th International Conference on Emerging Trends in Engineering & Technology, October 25th-27th, 2013, IETET (2013), pp 99-106.

[15] Mishra, A., Goel, A., Singh, R., Chetty, G., & Singh, L. (2012, June). A novel image watermarking scheme using extreme learning machine. In Neural Networks (IJCNN), The 2012 International Joint Conference on (pp. 1-6). IEEE.

[16] Miao, N., He, Y., & Dong, J. hymnMark: Towards Efficient Digital Watermarking on Android Smartphones.WORLDCOMP’12, ICWN’12: 2012, pp348-355

[17] Agarwal, C., Mishra, A., & Sharma, A. (2011, May). Digital image watermarking in DCT domain using fuzzy inference system. In Electrical and Computer Engineering (CCECE), 2011 24th Canadian Conference on (pp. 000822-000825). IEEE.

[18] R.C. Gonzalez, R.E. Woods and S.L. Eddins, Digital Image Processing Using MATLAB, Pearson Education (2005), pp 406 and 467.

[19] http://www.extreme-learning-machines.org/

[20] http://www.ntu.edu.sg/home/egbhuang/elm_codes.html

[21] http://source.android.com/

[22] http://developer.android.com/guide/topics/media/camera.html

Malarial Parasite Classification using Recurrent Neural Network

Muhammad Imran Razzak *razzakmu@ngha.med.sa*
Health Informatics, CPHHI
King Saud bi Abdulaziz University for Health Sciences
Riyadh, 11426, Saudi Arabia

Abstract

Malaria parasite detection relies mainly on the manual examination of Giemsa-stained blood microscopic slides whereas it is very long, tedious, and prone to error. Automatic malarial parasite analysis and classification has opened a new area for the early malaria detection that showed potential to overcome the drawbacks of manual strategies. This paper presented a method for automatic detection of falciparum and vivax plasmodium. Although, malaria cell segmentation and morphological analysis is a challenging problem due to both the complex cell nature uncertainty in microscopic videos. To improve the performance of malaria parasite segmentation and classification, segmented the RBC and used RNN for classification into its type. Segmented RBCs are classified into normal RBC and infected cell. RNN identify the infected cells into further types.

Keywords: Malaria Detection, Segmentation, RBC Classification, Blood Cell Analysis.

1. INTRODUCTION

Half of world population is at risk of life threatening infectious disease Malaria. It is a potentially fatal parasitic disease of both human and animals and causes 219, 216 million infection cases of malaria and killed 6.6, 6.5 million people in 2010 and 2011 respectively. The major population that is at high risk mainly includes pregnant women and children who especially under five years [1]. Since 2000, malaria mortality rates are reduced to more than 25% through increased prevention and control measure [2].

Malaria disease is transmitted via a bite from the infected female mosquito which introduce the organisms form her saliva. Five species of plasmodium can infect and be transmitted by human whereas the majority of deaths are caused by falciparum and vivax plasmodium. Species diagnose is necessary for proper treatment in case of malaria. Some rules for species identification are shown in Table 1. However it does not guarantee that every parasite will exhibit the morphological characteristics. Typically, the malarial infection can be diagnosed by microscopic examination of blood using blood films or with antigen based rapid diagnostic. Even after fifty years of malaria eradication program, it still continues to increase. Whereas the control tools are getting less effective due to drug and insecticide resistance that are developed in mosquitos. This alarming situation has led the researchers to develop a rapid, accurate and affordable diagnostic method for early malaria parasite detection [1]. Early detection of malaria is vital in order to ensure prompt and effective treatment. Patient suffering from malaria disease should be diagnosed at early stage and should be given an effective and affordable treatment within 24 hours [0]. Microscopic blood image analysis is a standard technique used for blood cell analysis for diagnosing, however in remote area, a delay in obtaining results may lead to incorrect initial treatment due to unavailability of early diagnose system.

Malaria parasite diagnoses is a manual counting process that use microscopic examination of Giemsa-stained thick and thin blood smears. Manual counting methods are very long, tedious and prone to technician's ability to conduct the process correctly that requires training and skills,

i.e. a trained expert takes about 15 min to evaluate and count 100 cells and blood sample of millions of patients is performed every year [4]. Manual blood cell counting is not a reliable screening method when it is performed by non-expert due to lake of training expertise as it requires special training and considerable expertise [5-8]. Machine aided automatic analysis of microscopic blood cell is a powerful diagnostic tool that improves accuracy, saves time and reduces the required manpower as well as minimizes human errors. Automatic malarial diagnose has larger interest especially for clinics and laboratories; however, blood cell segmentation and morphological analysis is a challenging problem due to both the complex cell nature and uncertainty in microscopic videos. Comparison of microscopy diagnosis and rapid diagnosis tests is shown in table 2.

Recognition and inspection of blood can assist hematologists in analyzing the blood sample and diagnosing diseases like Aids, malaria and blood cancer. Blood samples study has been widely researched in the field of immunology, infectious diseases, transplantation, hematological malignancy and vaccine development. Various numbers of algorithms and techniques have been published that are related to blood cell segmentation and classification. This paper presents a survey of algorithms particularly focusing on blood cell morphology and cell counting for automatic screening of several diseases.

An advance in genomic technologies has opened a new realm for early detection of diseases that shows potential to overcome the drawbacks of manual detection technologies. Automatic instrument for blood cell counting such as flow cytometry and automatic counting machines can examine cell quantity but not qualitatively. Yet 21% of blood samples analysis still requires microscopic expert review [9-10]. Camera based methods provides quantitative as well as qualitative blood evaluation whereas not extensive research has focused in this area [11]. Various works are going on analyzing the microscopic images to point out the infection presence in human blood. Thus, several image processing methods have been presented in literature for the automatic segmentation and classification of blood cell. This paper explores present malarial parasite identification and classification using recurrent neural network. The organization of the rest of the paper is as follow: Section II briefly reviews the malarial parasite recognition approaches discussed earlier and Section III presents methodology for the segmentation and classification of malarial infected cells whereas the conclusion and future directions are presented in section IV.

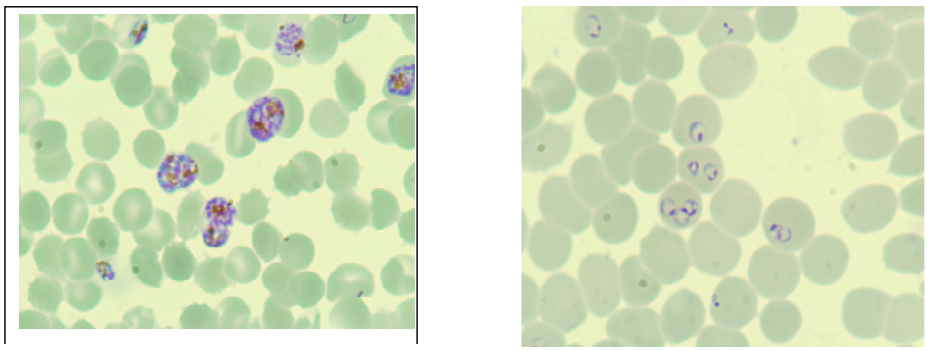

FIGURE 1: Malaria Effected Blood Images.

2. Related Work

Blood smear image consists of white blood cell, red blood cells, platelets as well as other possible contents such as malarial parasite, Aids virus etc. scattered across the background. The contents of blood cell images are very complex. The number or ratio of different blood cells in blood samples indicates different diseases, i.e. the white blood cells can be classified into more than 20 different classes according to their maturity [2]. Differential counting of blood cell can provide

valuable information for the accurate diagnosis of disease i.e. leukemia, cancer and other blood related diseases. Such differential counting involves classifying the blood cells with respect to color, size and shape. Blood cell counting is time consuming job for biologist, e.g. expert requires 15 min to count and evaluate a slide. Moreover, it is painstaking and subjective job which also requires training and skills. Due to these complexities and hematologist restrictions, manual counting accuracy decreases and thus machine based blood classification system is essential for biologist in diagnosing disease.

	P. Falciparum	P. Vivax	P. Ovale	P. Malariae
Size	Not enlarged	Enlarged	Enlarged	Enlarged
Shape	Round crescent gametocyte	Round or Oval	Round or Oval amoeboid	Round
Dots	Large red spots	Small red dots	Small red dots	Few tiny dots

TABLE 1: Some Rules for Species Identification.

An automated malarial diagnosis system can be designed by understanding the diagnostic expertise (hematologist knowledge) and representing it by specifically tailored image processing and pattern recognition algorithms. Image processing based malarial diagnostic methods has been widely studied in order to provide early and accurate detection of malaria parasite. An ideal diagnostic method would be accurate, non-invasive, and inexpensive. In order to perform malarial diagnosis, the system must be capable of differentiating between malaria infected cells, and healthy blood component. The key tasks for malarial parasite classification involve segmenting the malaria parasite infected cells from the complicated background.

There are many different methods for each phase that can be utilized to build machine based malarial parasite recognition system. We have discussed these approaches one by one in details. Most microscopes provide uniform or relatively uniform illumination images whereas several illumination and contrast enhancement technique have been applied in literature. One way to deal with uneven illumination is the predefined illumination correction but some time we don't have reference image [12]. Suradkar used the local histogram equalization for contrast enhancement of parasite and RBC [13] whereas Zou et al. and Sio et al. used adaptive histogram equalization [19] for image enhancement [14, 15]. Ruberto et al. used paraboloid modal for illumination correction [16]. Sriram et al. used diagonal modal for illumination modeling [17]. In diagonal modal, an image of unknown illumination is transformed to the known illuminant space by multiplying pixel values with a diagonal matrix. Das et al. performed gray world assumption for correcting illumination [18]. Nasir applied partial contrast stretching (PCS) to improve the image quality and contrast of malaria image. Diaz used adaptive local low-pass filter to correct luminance differences on luminance channel [20-21]. The filter was designed for a window size which contained the largest image feature, i.e. a typical erythrocyte size. Filter was selectively applied on higher luminance levels that represent the background pixels. Mehrjou used adaptive histogram shaping function for contrast enhancement [22]. The image is divided to several tiles and histogram shaping is applied to these tiles separately followed by bilinear interpolation to eliminate artificially induced boundaries.

In some cases, the illumination can be excessively uneven thus the use of histogram, adaptive Otsu etc may not work sometime. Sabino et al. performed non-supervised nucleus region detection before nucleus color segmentation using the G channel from RGB color coordinates [23]. For colored images segmentation into ROIs, supervised classification method that is based on RGB color space is used. Costa et al.minimizes the sensibility of cytoplasm to small color variations using cell-modeling and morphological filters [24], an alternative for noise reduction of transformation from color images to segmented ROIs.

Memeu et al. used both RGB and HIS for segmentation [425]. Green channel from RGB whereas hue and saturation channels are used for segmentation based on Otsu method and Zack algorithms for RBC and parasites respectively. The green channel gave good results for erythrocytes segmentation but it also added the parasite as part of the foreground. The hue

component resulted to a binary image whose foreground had noisy boundaries whereas the saturation component failed to produce erythrocytes as the objects.

Kaewkamnerd et al. segmented the background by using histogram on to HSV color format [26]. After background segmentation, the image is divided into small windows of 300 by 300 pixels for efficient processing. Finally, malaria parasites are identified based on their size. Sriram et al. segmented the background by using histogram on green component RGB color format [17].

Multilevel thresholding especially using Otsu method has been performed by many researchers for blood cell segmentation and it showed promising results. Savkare and Narote performed Global threshold and Otsu thresholdding on gray scale and green channel image [27]. Both images are added and median filter is applied to remove the unwanted points. Later on distance transform and watershed transform are applied to segment the cells. Kumar et al. used Otsu threshold on histogram of B component of RGB color space followed by the morphological operation [28]. Ahirwar et al. relied on two thresholds (one for erythrocytes, and one for parasites) for parasite segmentation [29]. The first threshold is selected to separate the erythrocytes from the background of the image. The second threshold is taking the first minimum after the principal mode of the histogram incorporating only the erythrocytes. Tek et al. modeled the stained and unstained pixel distributions with histograms and used the probability densities to determine whether a pixel on the input image is stained or not [12].

	Microscopy	**RDTs**
Requirement	Electricity Special Training Staining Chemical	None, Basic Training, None
Time	~60 Minutes	15-20 Minutes
Cost		
	Specification	
Detection Threshold	50 pal/ul	~100par/ul
Detection of all species	Yes	Some bands
Quantification	Yes	None
Specie Identification	Yes	None
Life Stage Identification	Yes	None

TABLE 2: Comparison of Microscopy Diagnosis and Rapid Diagnosis Tests [34].

3. Malarial Parasite Detection: Methodology

An automated malarial diagnosis system can be designed by understanding the diagnostic expertise (hematologist knowledge) and representing it by specifically tailored image processing and pattern recognition algorithms. Image processing based malarial diagnostic methods has been widely studied in order to provide early and accurate detection of malaria parasite. An ideal diagnostic method would be accurate, non-invasive, and inexpensive. In order to perform malarial diagnosis, the system must be capable of differentiating between malaria infected cells, and healthy blood component. The key tasks for malarial parasite classification involve segmenting the malaria parasite infected cells from the complicated background. There are three major steps of analyzing malarial parasite infected images.

- Preprocessing
- Segmentation
- Classification

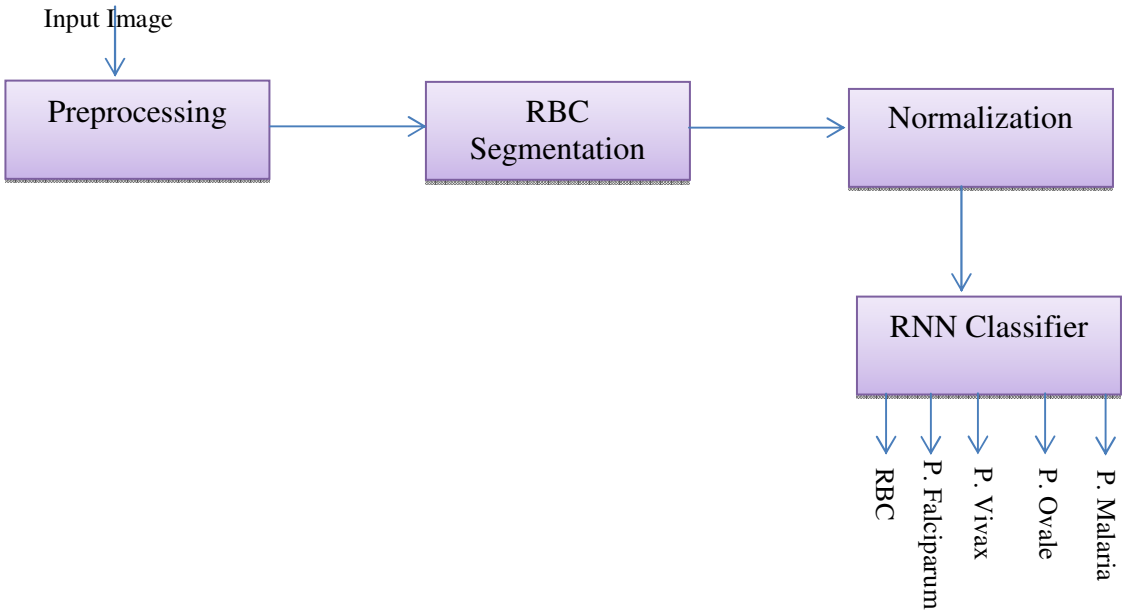

FIGURE 2: Malaria Parasite Classification [30].

2.1 Preprocessing

The aim of preprocessing is to obtain images with low noise, high contrast than original images for the further processing. Due to camera calibration and staining variability of blood smear, changes may occur in illumination and color distribution of blood images. This particular problem poses difficulties for classification of blood cells since it is hard to deal with proper segmentations of objects with quite similar colors. This process contains two operations image enhancement and noise reduction. We have used spatial filtering (median filter) for noise reduction. The median filter replaces pixel value with the median of its neighboring value.

To get the finest coefficients details of noise free image, a Forward Discrete Curvelet Transform (FDCT) is applied to the V channel as shown in Figure 3(b). It is a multi-dimensional transformation which can sense both the contours as well as curvy edges of the overlapping objects in the image. The FDCT has high directional sensitivity along with the capability to capture the singularities. Edge and singularity details are processed to extract the feature. After obtaining the highest detailed coefficients Inverse Discrete Curvelet Transform is applied to high frequency band to obtain the detailed image. This detailed image is now having the stronger edges than the original and would perform better in lending edge details to the segmentation step.

The next step is the adaptive equalization operation to spread out the intensity values along the total ranges of values in order to achieve better contrast. Adaptive histogram equalization differ from ordinary histogram equalization in respect that it computes several histogram of each corresponding to distinct section and use these histogram to redistribute the lightness value. After applying the adaptive histogram equalization, the background pixels have higher intensities than the cells.

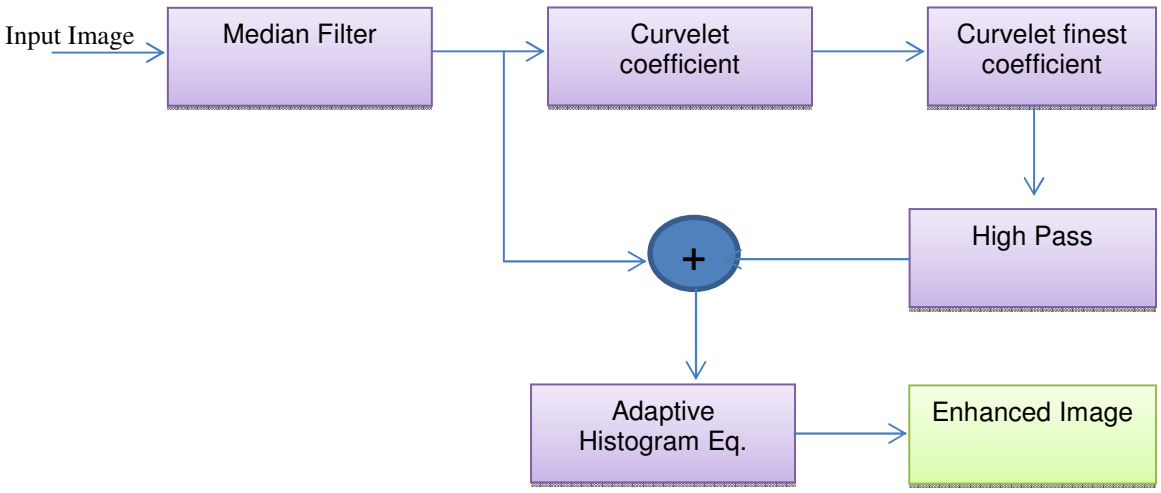

FIGURE 3: Preprocessing of Blood Cell Image.

2.2 Segmentation

In the analysis of automatic classification of malarial parasite procedures, the most important and difficult part is segmentation of malaria parasite infected blood cells from the background and other cells because the blood cells are often overlaid with each other and is the basis of quantitative analysis of its deformability and hence its filterability[12]. Cell shapes, light variation and noise are the other factors that make segmentation a difficult task. Accurate segmentation allows fruitful result in sub-sequent levels. Malarial parasite lies in erythrocytes thus we need to segment the erythrocyte form the blood images. We have used Rao's method for background segmentation. Rao's method extracts a rough foreground image using morphological rea top-hats. Two different threshold values are determined form these backgrounds and foreground that are used to produce the refined binary foreground mask.

At the end, a box counting algorithm is used to the segmented the blood cell images. The box counting algorithm counts the number of blood cells boxes having side length r needed to cover the surface of fractal objects and the number of boxes N, occupied by more than one pixel of the image. We have defined two procedures by two parameters for box counting. First one is the selection of r whereas the second is the range of r. The blood cell image has finite set of points and the upper limit is the image size while the lower is the pixel unit. Various researches propose using 2, 4, 8, 16, 2n pixels as box sizes to have a uniform spread of observation. The quadratic boxes cover the object, and the number of the boxes is recorded. The fractal dimension (FD) measures the dependence between the number of boxes N and the box side length r.

2.3 Classification of Malarial Parasite

We have used recurrent neural networks (RNN) for classification of the malarial parasite. RNNs are the computational modals that simulated structure and function of biological neural networks. Training is an important task in utilizing the neural network.

The BLSTM Network

We employed Bidirectional Long Short Term Memory (BLSTM) networks for the detection and classification of malarial parasite into four types. The BLSTM is a Recurrent Neural Network (RNN) approach to learn the sequential patterns. For maintaining the sequence, it is important to use previous computations at current point in time. In addition to that the future point should be predicted by keeping the current and previous calculations. It means RNN can also work in a bidirectional way. The bidirectional feature of RNN makes it vulnerable for learning patterns. The RNN is primarily meant to deal with sequences but it has a limit that not to deal with complex and

large sequences. As RNN iteration proceeds, the previous computation becomes faded with increase in time lag. But it can be the situation if we require the most previous computation at current point in time then it would be difficult to have that particular computation. The LSTM memory cell is depicted in Figure 6.

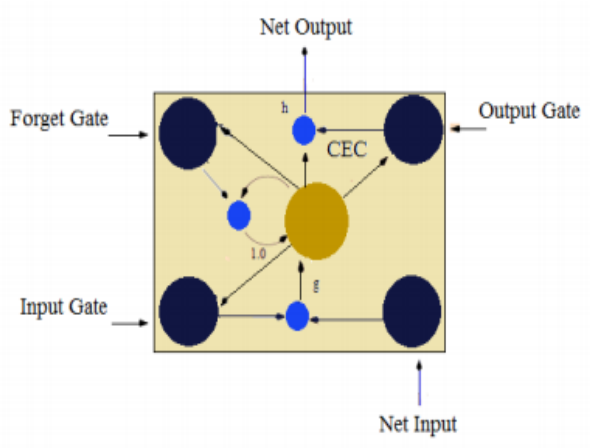

FIGURE 4: LSTM Memory Cell.

Training

We have segmented each Red blood cell using the bounding box in previous section. The RBC image is normalized to LxM size for RNN. We have five types of classes i.e. RBC, R.Falciparum, P.Vivax, P. Ovale and P. Malaria and the RNN is trained on these five types of cells. This normalized segmented RBC image with their corresponding ground truth (RBC, R.Falciparum, P.Vivax, P. Ovale and P. Malaria) is given to BLSTM classifier individually. The classifier then computes training and validation errors in series of epochs. In every epoch the classifier computes the forward pass in addition to backward pass. After every epoch the training and validation errors were computed and stored with the best results. When there is no significant change in training and validation error computation then training terminates. The training and validation were saved and used for testing phase. There are four parameters (like input image size, hidden layer neurons, learning rate and momentum) which we can tune them to produce variation in results. But in our experiments the momentum, learning rate and image size kept fixed. The only tuning parameter is number of hidden layer neurons. We reported the best results that have produced on 120 memory cells in hidden layer.

BPNN	RBC	P. Falciparum	P. Vivax	P. Ovale	P. Malariae
RNN	98.2	92.6	93.2	94.1	96.5

TABLE 3: Recognition Result.

Testing

We have five types of classes i.e. RBC, R.Falciparum, P.Vivax, P. Ovale and P. Malaria. The RNN is trained on these five types of cells. The normalized segmented red blood cell is forward to RNN for classification into one of five types (RBC in case of not infected and other four types in case of malarial infected cell).

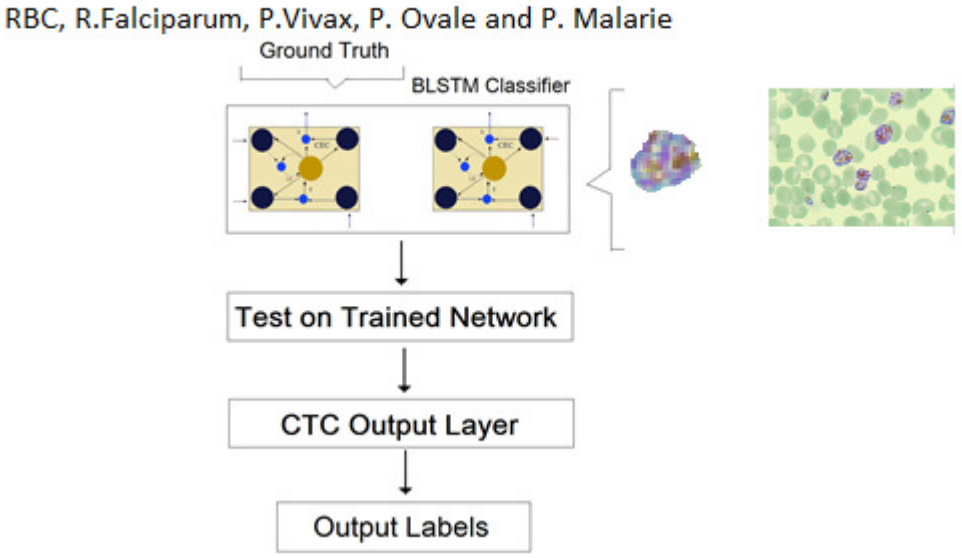

FIGURE 5: RNN for Malarial Parasite Classification.

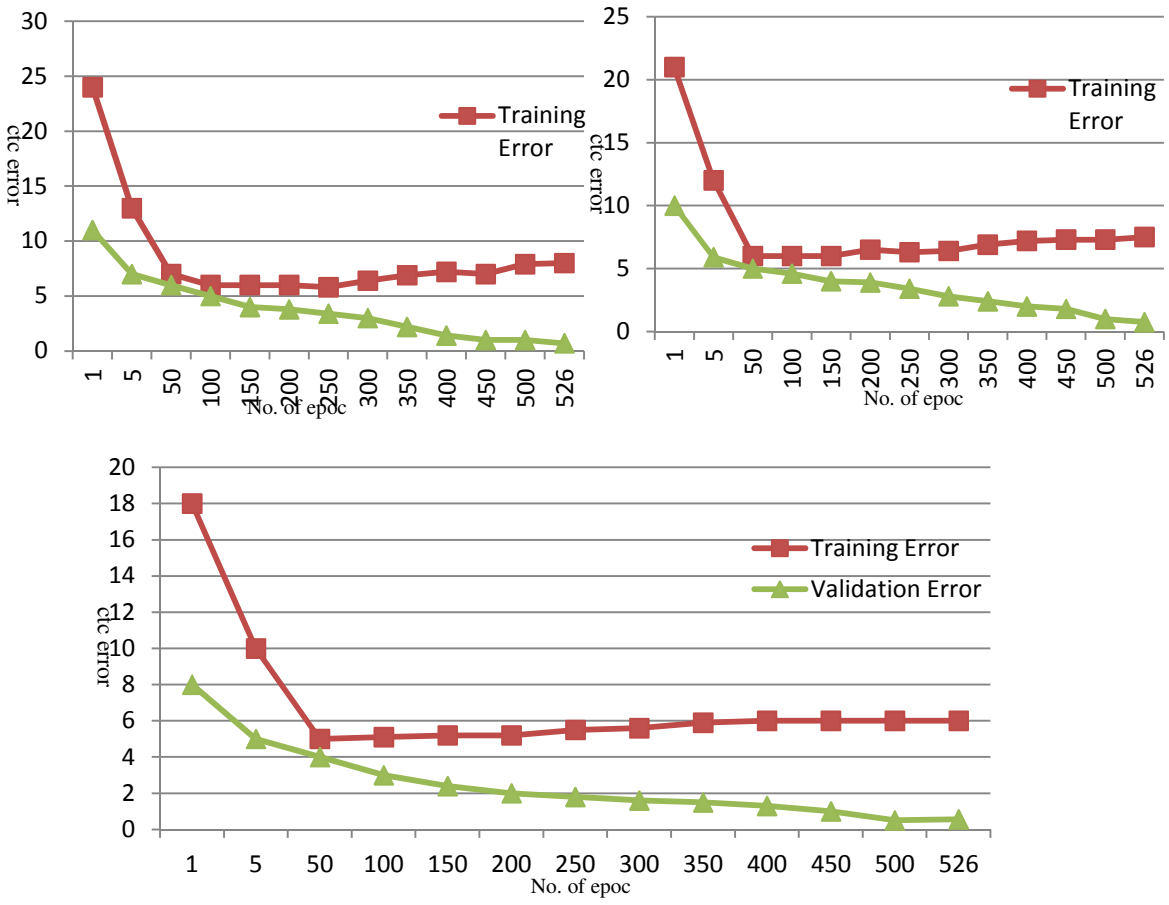

FIGURE 6: Learning sequences on various (a=60, b=80, c=120) LSTM memory cells.

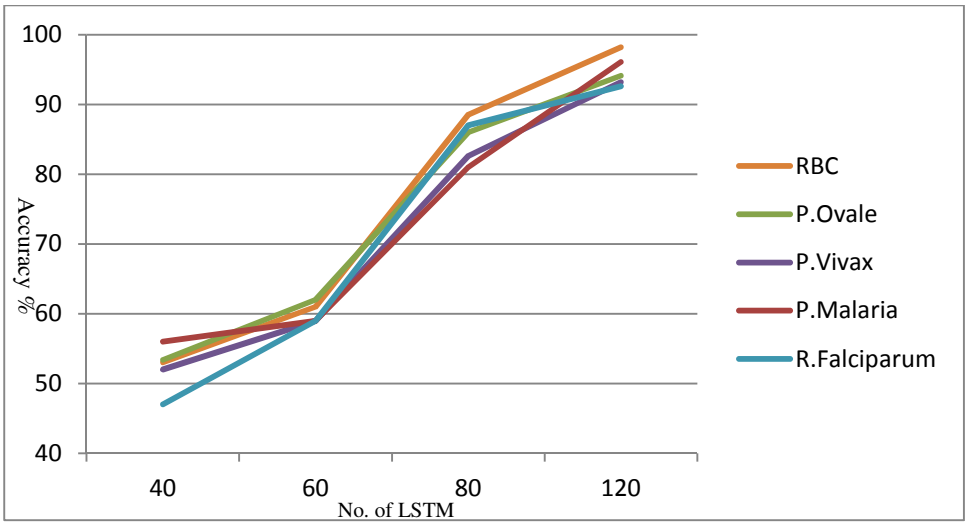

FIGURE 7: Accuracy and no of LSTM.

4. CONCLUSION

The paper presented a method for automatic detection of falciparum and vivax plasmodium. Although, malaria cell segmentation and morphological analysis is a challenging problem due to both the complex cell nature uncertainty in microscopic videos. To improve the performance of malaria parasite segmentation and classification, we have extracted the red blood cells and forward to Recurrent neural network for further classification into five types RBC, R.Falciparum, P.Vivax, P. Ovale and P. Malaria. RNN provided 98.2%, 92.6%, 93.2%, 94.1% and 96.1%, respectively for RBC, R.Falciparum, P.Vivax, P. Ovale and P. Malaria.

5. REFERENCES

[1] Yunda L., Ramirez, A.A., Millan, J., Automated Image Analysis Method for p-vivax Malaria Parasite Detection in Thick Film Blood Images, Revista S&T, 10(20), 9-25

[2] World Health Organization: World Malaria Report 2011. Geneva; 2011

[3] Chan LL, Laverty DJ, Smith T, Nejad P, Hei H, Gandhi R, Kuksin D, Qiu J., Accurate measurement of peripheral blood mononuclear cell concentration using image cytometry to eliminate RBC-induced counting error" , Journal of Immunological Method, Vol. 238, pp 25-32, 2013 Feb

[4] Chan, Y.-K., Tsai, M.-H., Huang, D. C., Zheng, Z.-H., Hung, K.-D., 2010. Leukocyte nucleus segmentation and nucleus lobe counting. BMC Bioinformatics 11, 558.

[5] M. M. Kettelhut, P. L. Chiodini, and H. Edwards, Moody A: External quality assessment schemes raise standards: evidence from the UKNEQAS parasitology subschemes. J. Clin. Pathol. 56, 927 (2003).

[6] R. E. Coleman, N. Maneechai, N. Rachaphaew, C. Kumpitak, R. Miller, V. Soyseng, K. Thimasarn, and J. Sattabongkot, Comparison of field and expert laboratory microscopy for active surveillance for asymptomatic plasmodium falciparum and plasmodium vivax in western thailand. Am. J. Trop Med. Hyg. 67, 141 (2002).

[7] Bates, V. Bekoe, and A. Asamoa-Adu, Improving the accuracy of malaria related laboratory tests in Ghana. Malar J. 3, 38 (2004).

[8] K. Mitiku, G. Mengistu, and B. Gelaw, The reliability of blood film examination for malaria at the peripheral health unit. Ethiopian J. of Health Dev. 17, 197 (2003).

[9] T. Chen, YongZhang, C. Wang, ZhenshenQu, FeiWang, and Tanveer Syeda-Mahmood, Complex local phase based subjective surfaces (CLAPSS) and its application to DIC red blood cell image segmentation. Neurocomputing 99, 98 (2013).

[10] M.I.Razzak, B. AlHaqbani, "Automatic Detection of Malarial Parasite Using Microscopic Blood Images" Journal of Medical Imaging and Health Informatics Vol. 5, 1–8, 2015

[11] S. H. Rezatofighti and H. Soltanian-Zadeh, Automatic Recognition of Five types of White blood cell in peripheral blood. Computerized Medical Imaging and Graphics, Volume 35, Issue 4, Pages 333–343, June 2011.

[12] F. B. Tek, A. G. Dempster, and I. Kale, Malaria parasite detection in peripheral blood images. Proceeding of British Machine Vision Conference (2006).

[13] T. P. Suradkar, Detection of malarial parasite in blood using image processing. International Journal of Engineering and Innovative Technology (IJEIT) 2, (2013).

[14] M. I. Khan, B. Acharya, B. K. Singh, and J. Soni, Content based image retrieval approaches for detection of malarial parasite in blood images. International Journal of Biometrics and Bioinformatics (IJBB) 5 (2011).

[15] W. S. Selena Sio, W. Sun, Saravana Kumar, W. Z. Bin, S. S. Tan, S. H. Ong, H. Kikuchi, Y. Oshima, and K. S. W. Tan, Malaria Count: An image analysis-based program for the accurate determination of parasitemia. Journal of Microbiological Methods 68, 11 (2007).

[16] C. D. Ruberto, A. Dempster, and S. B. Khan Jarra, Analysis of infected blood cell images using morphological operators. Image and Computer Vision 20 (2002).

[17] R. Sriram, M. Chandar, and K. Srinivas, Computer aided malarial diagnosis for JSB stained white light images using neural networks. International Journal of Advanced Research in Computer Science and Software Engineering 3 (2013).

[18] D. K. Das, M. Ghosh, M. Pal, A. K. Maiti, and C. Chakraborty, Machine learning approach for automated screening of malaria parasite using light microscopic images. Micron 45, 97 (2013).

[19] Z. Karel, Contrast limited adaptive histogram equalization. Graphics Gems IV 474–485 (1994), (code: 479–484).

[20] G. Díaz, F. A. González, and E. Romero, A semi-automatic method for quantification and classification of erythrocytes infected with malaria parasites in microscopic images. Journal of Biomedical Informatics 42, 296 (2009).

[21] Gloria Díaz, Fabio Gonzalez, and Eduardo Romero, Infected cell identification in thin blood images based on color pixel classification: Comparison and analysis. Lecture Notes in Computer Science 4756, 812 (2007).

[22] A. Mehrjou and T. Abbasian, Automatic Malaria Diagnosis System, First International Conference on RSI/ISM.

[23] D. M. U. Sabino, L. da Fontoura Costa, E. Gil Rizzatti, and M. Antonio Zago, A texture approach to leukocyte recognition. Real-Time Imaging 10, 205 (2004).

[24] F. Costa L da and R. Marcondes, Jr., Shape analysis and classification: theory and practice. Boca Raton, FL: CRC Press (2001).

[25] D. M. Memeu, K. A. Kaduki, and A. C. K. Mjomba, Njogu Samson Muriuki,Lucy Gitonga, Detection of plasmodium parasites from images of thin blood smears. Open Journal of Clinical Diagnostics 3, 183 (2013).

[26] S. Kaewkamnerd and C. Uthaipibull, Apichart Intarapanich, Montri Pannarut, Sastra Chaotheing, Sissades Tongsima, An automatic device for detection and classification of malaria parasite species in thick blood film. BMC Bioinformatics 13, S18 (Suppl 17) (2012).

[27] S. S. Savkare and S. P. Narote, Automatic detection of malaria parasites for estimating parasitemia. International Journal of Computer Science and Security (IJCSS), 5 (2011).

[28] A. Kumar, A. Choudhary, P. U. Tembhare, and C. R. Pote, Enhanced identification of malarial infected objects using otsu algorithm from thin smear digital images. International Journal of Latest Research in Science and Technology ISSN (Online):2278-5299, 1, 159 (2012).

[29] N. Ahirwar, S. Pattnaik1, and B. Acharya, Advanced image analysis based system for automatic detection and classification of malarial parasite in blood mages. International Journal of Information Technology and Knowledge Management 5, 59 (2012).

[30] Muhammad Imran Razzak, “Automatic Detection and Classification of Malarial Parasite”, International Journal of Biometrics and Bioinformatics (IJBB) Volume-9 Issue-1, 2015

Sine and Cosine Fresnel Transforms

Habib Hamam *Habib.Hamam@umoncton.ca*
Faculty of Engineering,
Université de Moncton, NB, E1A 3E9, Canada
and Canadian Institute of Technology, Tirana, Albania

Abstract

Two novel transforms, related together and called Sine and Cosine Fresnel Transforms, as well as their optical implementation are presented. Each transform combines both backward and forward light propagation in the framework of the scalar diffraction approximation. It has been proven that the Fresnel transform is the optical version of the fractional Fourier transform. Therefore the former has the same properties as the latter. While showing properties similar to those of the Fresnel transform and therefore of the fractional Fourier transform, each of the Sine and Cosine Fresnel transforms provides a real result for a real input distribution. This enables saving half of the quantity of information in the complex plane. Because of parallelism, optics offers high speed processing of digital signals. Speech signals should be first represented by images through special light modulators for example. The Sine and Cosine Fresnel transforms may be regarded respectively as the fractional Sine and Cosine transforms which are more general than the Cosine transform used in information processing and compression.

Keywords: Diffraction, Fresnel Transform, Fractional Fourier Transform, Cosine Transform, Sine Transform.

1. INTRODUCTION

The fractional order Fourier transform shows interesting properties [1] and has been used in various domains [2-5] including information processing and compression [3,4]. This transform is very useful in both computer-based (including DSP and FPGA) or optics-based signal processing. The fractional Fourier transform is more general than the Fourier transform since the former transforms a time (or space) domain signal into a time-frequency domain in the same way. In other words, fractional Fourier domains correspond to oblique axes in the time-frequency plane.

An optical implementation of the fractional Fourier transform has been proposed [5-7]. It has been proven that the Fresnel transform as defined by reference [1] is the formulation of the optical version of the fractional Fourier transform [6,7].

The Fourier transform of a real distribution is generally complex. A particular case occurs when the initial real distribution is even, since such a distribution is Fourier transformed into an even real distribution. However the Cosine transform, which is derived from Fourier transform, transforms any real distribution into a real distribution (spectrum). For this reason, the Cosine transform is used more than the Fourier transform in signal and image compression. The famous JPEG format is a typical example.

The Fresnel transform generally transforms real distributions, no matter they are even or not, into complex distributions. In this paper, we will present a new transform derived from the Fresnel transform that behaves like the Cosine transform with respect to real distributions. This transform is referred to as the Cosine Fresnel transform. In a similar way, we will define the Sine Fresnel transform.

While showing properties similar to those of the Fresnel transform and therefore to those of the fractional Fourier transform, each of the Sine and Cosine Fresnel transforms provides a real result for real input distributions. This enables saving half of the quantity of information. The Sine and Cosine Fresnel transform may be regarded respectively as the fractional Sine and Cosine transforms which are more general than the Cosine transform used in information processing and compression. In other words, the main interest of the two new transforms, proposed in the present paper, lies in the fact that they combine the advantages of the fractional Fourier transform with the advantages of the Cosine transform.

We also present an optical implementation of these two transforms. The advantage of optics is the high speed of processing of digital signals. Although derived from the same transform, namely the Fresnel transform, and the only mathematical difference lies in using sine and cosine functions respectively, the Sine and Cosine Fresnel transforms show some distinct behaviors that we will expose in the discussion.

The remainder of the paper will be organized as follows: After the present introduction, section 2 will be devoted to the Fresnel transform. Then, the Cosine Fresnel transform will be defined in section 3, followed by the Sine Fresnel transform. In section 4, the optical implementation of these transforms will be addressed. The section 5 presents some experimental illustrations that will be used in the discussion of section 6. Concluding remarks will be given in section 7.

2. FRESNEL TRANSFORM

The Fresnel transform models diffraction in the Fresnel zone as well as in the Fraunhofer zone. Hence, the diffraction field observed at a distance z behind an object is [1]:

$$h(x,z)=\frac{\exp\left(i2\pi z/\lambda\right)\exp(-i\pi/4)}{\sqrt{\lambda z}}h(x)*f_k(x,z) \tag{1}$$

For brevity of notation, the analysis is limited to the one-dimensional consideration. h(x)=$h(x,z=0)$ is the initial field just behind the object, and * denotes convolution. The Fresnel kernel is expressed as follows:

$$f_k(x,z)=\exp\left(j\pi\frac{x^2}{\lambda z}\right) \tag{2}$$

Also for brevity of notation, the constant term of propagation $\exp\left(j2\pi z/\lambda\right)$ and the constant phase shift factor $\exp(-j\pi/4)/\sqrt{\lambda z}$ will be ignored, λ is the illuminating wavelength. Equation (1) results from an assumption that enables treating light as a scalar phenomenon where the components of either the electric or magnetic field can be treated independently in a similar way [8].

The convolution form of Equation (1) is expanded as follows:

$$h(x,z)=\exp\left(j\frac{\pi}{\lambda z}x^2\right)\int_{-\infty}^{+\infty}\exp\left(j\frac{\pi}{\lambda z}x_1^2\right)h(x_1,0)\exp\left(-2j\frac{\pi}{\lambda z}x_1x\right)dx_1 \tag{3}$$

3. SINE AND COSINE FRESNEL TRANSFORMS

Although $h(x)$ may be real, $h(x,z)$ is generally not real because the Fresnel kernel is complex. The idea is to propose a new kernel by taking only the real part of the Fresnel kernel:

$$f_C(x,z)=\frac{f_k(x,z)+f_k(x,-z)}{2}=\cos\left(\pi\frac{x^2}{\lambda z}\right) \tag{4}$$

This leads to a new transform that we call Cosine Fresnel transform. The result $h_C(x,z)$, observed at a distance z, is expressed as follows:

$$h_C(x,z) = h(x) * f_C(x,z) = \frac{h(x,z) + h(x,-z)}{2} \tag{5}$$

Thus, the Cosine Fresnel transform is the average of the diffraction field at distance z (wave moving forwards) and the diffraction field at distance -*z* (wave moving backwards). Therefore, the Cosine Fresnel transform has similar properties as the Fresnel transform itself. The advantage is that Cosine Fresnel transform is real for an initial real distribution. Analogy may be done with the relationship between the Fourier transform and the Cosine transform. Since the Fourier transform is complex, the Cosine transform, which is real, is used more than the former in image compression. The famous JPEG format is a typical example.

Similarly we can define the Sine Fresnel transform $h_S(x,z)$, observed at a distance z , as follows:

$$h_S(x,z) = h(x) * f_S(x,z) = \frac{h(x,z) - h(x,-z)}{2j} \tag{6}$$

With

$$f_S(x,z) = \frac{f_k(x,z) - f_k(x,-z)}{2j} = \sin\left(\pi \frac{x^2}{\lambda z}\right) \tag{7}$$

Let us express the Cosine Fresnel transform in the spatial frequency domain by Fourier transforming Equation (5):

$$H_C(u,z) = H(u,0) \times F_C(u,z) \tag{8}$$

where $H(u,0)$ is the Fourier transform of the initial field $h(x,0)$, $H_C(u,z)$ is the Fourier transform of the Cosine Fresnel transform $h_C(x,z)$, and $F_C(u,z)$ is the Fourier transform of the Cosine Fresnel kernel of Equation (4). By looking at the table of Fourier transform pairs, for example in [1], we find:

$$F_C(u,z) = \sqrt{\lambda z}\cos\left(-\pi\lambda z u^2 + \pi/4\right) \tag{9}$$

For the Sine Fresnel transform, we also obtain an even real function, namely:

$$F_S(u,z) = \sqrt{\lambda z}\sin\left(-\pi\lambda z u^2 + \pi/4\right) \tag{10}$$

The phase shift factor of π/4 as well as the multiplicative factor $\sqrt{\lambda z}$ in Equations (9) and (10) are in fact compensated by respectively the real and imaginary part of the constant phase shift factor that we ignored above, namely exp(-jπ/4)/ $\sqrt{\lambda z}$. The remaining terms of Equations (9) and (10), namely $\cos\left(-\pi\lambda z u^2\right)$ and $\sin\left(-\pi\lambda z u^2\right)$ respectively, show interesting properties. For example, self-imaging related properties will be detailed in a future publication with some applications.

We can also express the Sine and Cosine Fresnel transform in a form similar to Equation (3):

$$h_C(x,z) = \int_{-\infty}^{+\infty} h(x_1,0)\cos\left(\frac{\pi}{\lambda z}(x-x_1)^2\right)dx_1 \tag{11}$$

and

$$h_S(x,z) = \int_{-\infty}^{+\infty} h(x_1,0)\sin\left(\frac{\pi}{\lambda z}(x-x_1)^2\right)dx_1 \tag{12}$$

The Sine and Cosine Fresnel transforms are equivalent to the fractional Fourier transform since both of them transform a time (or space) domain signal into a time-frequency domain in the same

way. In other words, fractional Fourier domains correspond to oblique axes in the time-frequency plane.

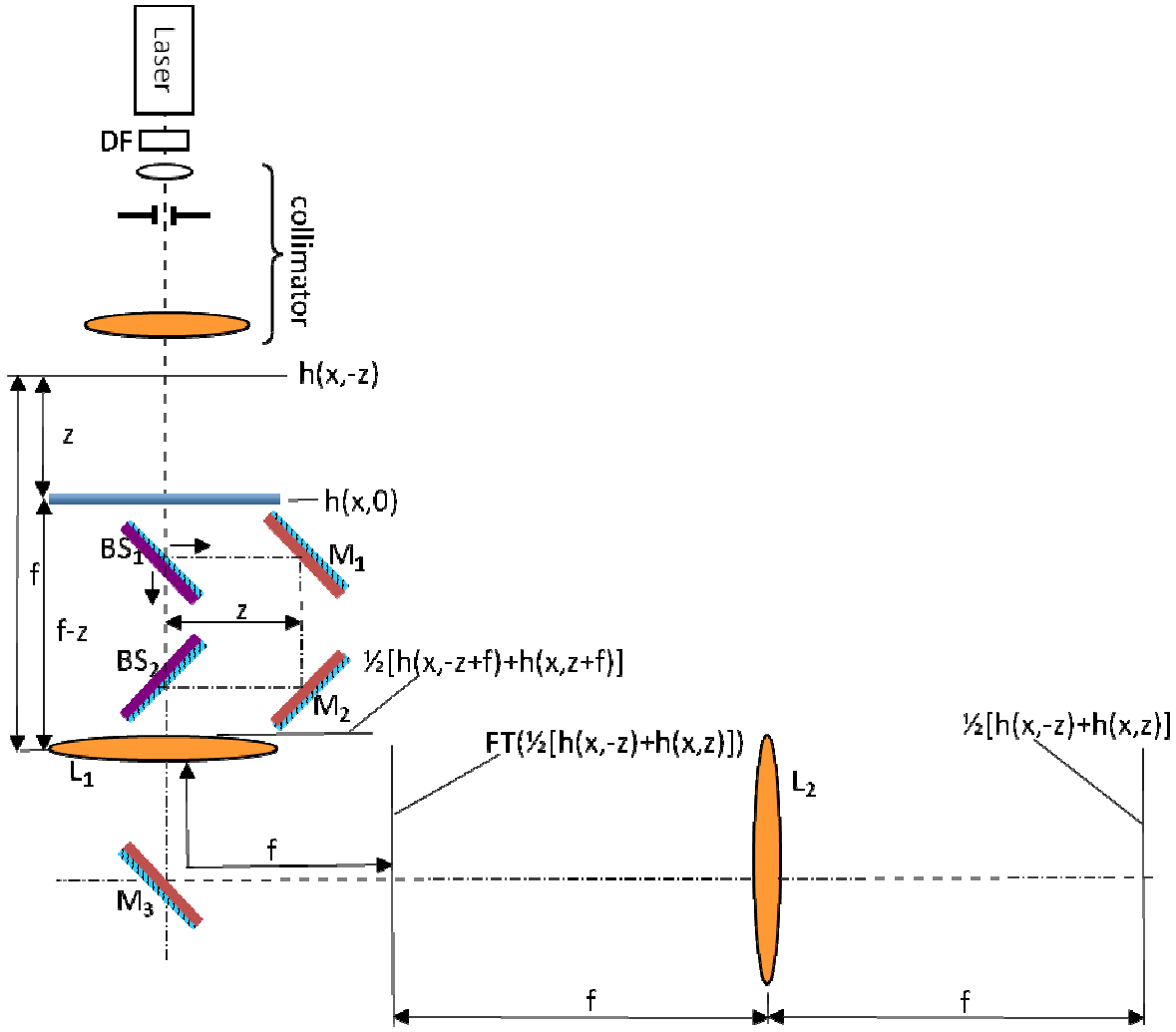

FIGURE 1: A setup to implement the Cosine Fresnel transform optically: a 4-f setup enables reobserving the field $h(x,-z)$ at the back focal plane of the second lens. A beam-splitter BS_1 replicates the field $h(x,0)$ into two replicas. One of the replicas covers an additional distance of $2z$ with respect to the other replica. The two lenses of the 4-f setup may be placed before the creation of replicas as in Figure 2. To obtain the Sine Fresnel transform, we should insert a plate to cause a delay of $\lambda/2$ in one of the arms between the two beam splitters BS_1 and BS_2 as in Figure 2.

In our previous formulas, we considered the space variable *x*, but the analysis is valid for the time variable *t*. It is worth noting that the Fresnel transform is also used to formulate chromatic dispersion in single mode fiber where instead of using the space variable *x*, the time variable t is used [9, 10]. This similarity also let to the Talbot effect in both space and time domain [10,11].

The fractional Fourier transform is expressed as follows for a fractional parameter α [5,6]:

$$h_s(x,z) = \int_{-\infty}^{+\infty} h(x_1,0)\sin\left(\frac{\pi}{\lambda z}(x-x_1)^2\right)dx_1 \qquad (13)$$

with $\csc(\alpha) = 1/\sin(\alpha)$. We see the similarity between Equations (3) and (11).

4. OPTICAL IMPLEMENTATION

The Fresnel transform is implemented naturally by diffraction in the Fresnel zone as well as in the Fraunhofer zone. To optically implement the Sine and Cosine Fresnel transforms, we propose two similar optical setups as depicted in Figures 1 and 2. As will be explained, each of the setups may be used for either transform by adding or omitting a transparent plate to cause a delay of λ/2.

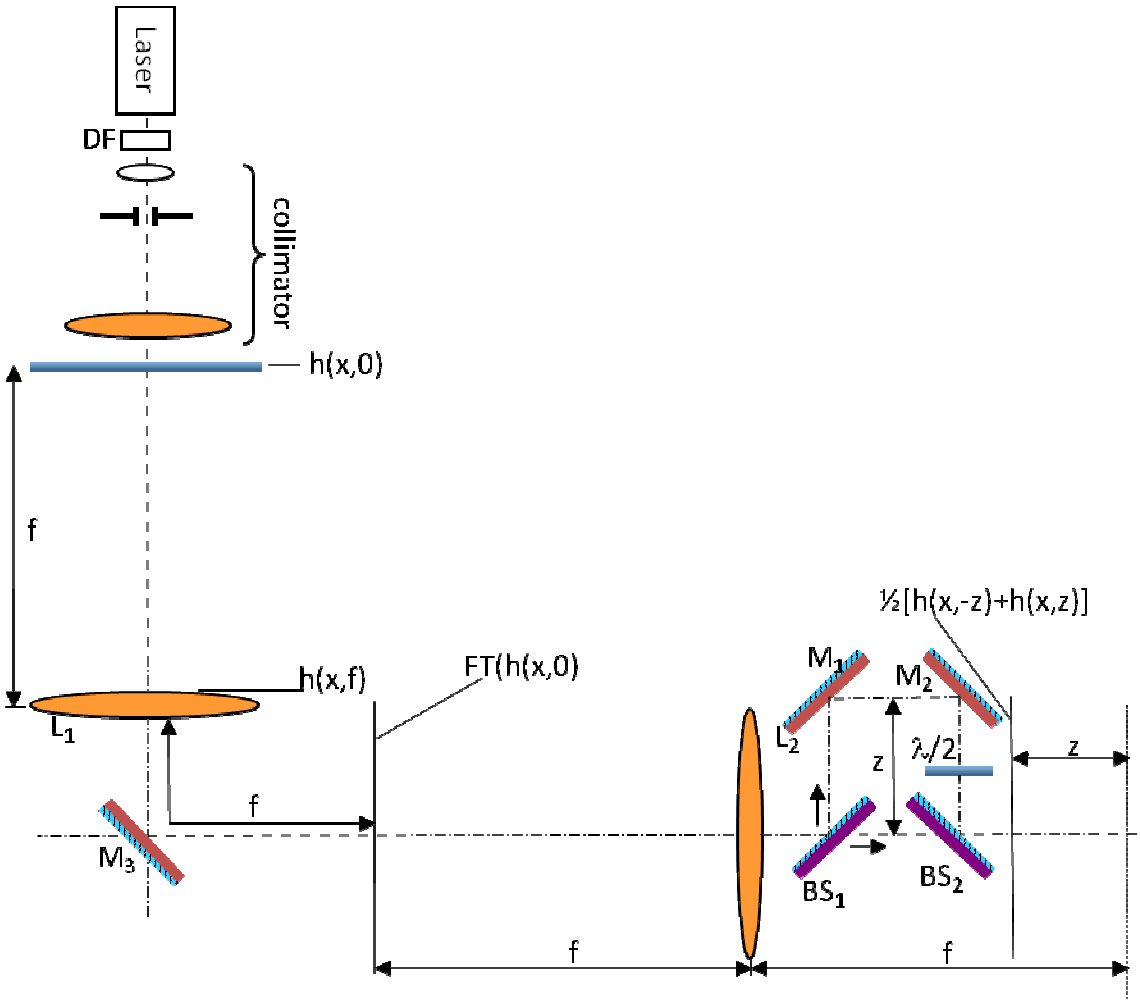

FIGURE 2: An optical setup to implement the Sine Fresnel transform that is identical to Figure 1, except that the two lenses of the 4-f setup is placed before the creation of replicas. Moreover, a plate is inserted to cause a delay of λ/2 in one of the arms between the two beam splitters BS1 and BS2. To obtain the Cosine Fresnel transform, the plate should be omitted.

The idea of both setups is the following: a 4-f setup enables reobserving the initial field at the back focal plane of the second lens. As depicted in Figure 1, we replicate the intermediate diffraction field by means of a beam-splitter BS_1. One of the replicas will cover an additional distance of $2z$ with respect to the other replica. If one replica goes through both converging lenses and covered the distance 4f-z, then it will have the same expression as the field which propagates backwards by a distance z. Thus we obtain ½ $h(x,-z)$. The other replica covers the distance 4f-z+2z=4f+z and is then expressed by ½ h(x,z). In reality, we observe, at the output of the 4-f setup, the mirrored version of a given input field $g(x,0)$, namely $g(-x,0)$. This detail is ignored for the sake of simplicity. Thus in the back focal plane of the second lens, we observe ½ $[h(x,-z)+h(x,z)]$, which is the Cosine Fresnel transform of $h(x)$ as expressed by Equation (5). The expressions of the intermediate fields are given in Figure 1. It is worth noting that the distance z

should not be so big that mutual coherence between the two light beams, superimposed by means of the second beam splitter BS_2, is lost.

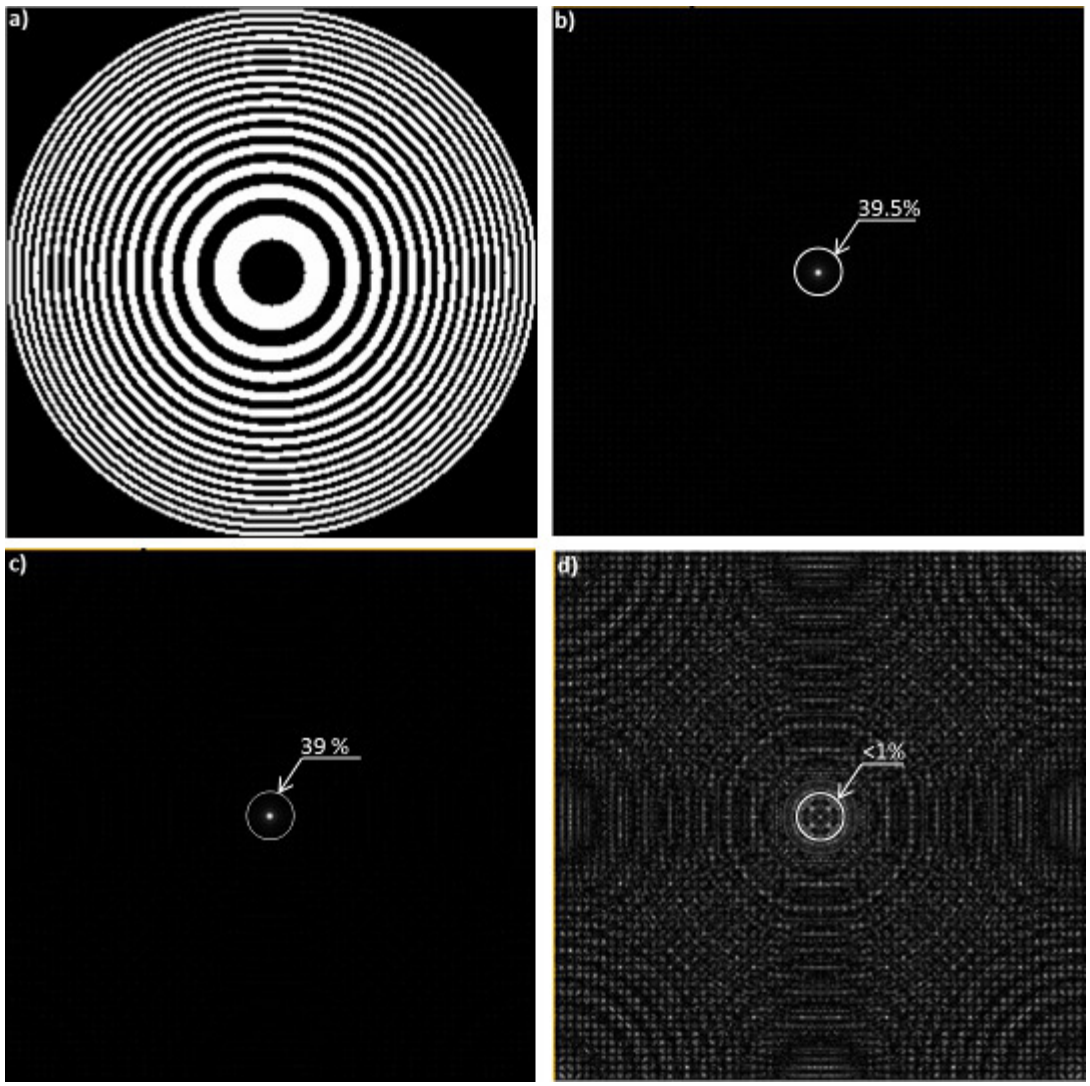

FIGURE 3: Simulation results: a) diffraction object: binary phase only Fresnel zone plate, b) The diffraction pattern at the back focal plane of this binary lens, 39.5% of the light is focused in a point, c) Sine Fresnel transform of the binary lens observed in its back focal plane, 39% of the light is focused in a point, d) Cosine Fresnel transform of the same lens observed in its back focal plane.

Figure 2 presents a setup implementing the Sine Fresnel transform. The setup is identical to that of Figure 1, except that the two lenses of the 4-f setup are placed before the creation of replicas. Moreover, a plate is inserted to cause a delay of $\lambda/2$ in one of the arms between the two beam splitters. To obtain the Cosine Fresnel transform, the plate should be omitted. Similarly, to obtain the Sine Fresnel transform based on the setup of Figure 1, we should insert a plate to cause a delay of $\lambda/2$ in one of the arms between the two beam splitters as in Figure 2.

5. EXPERIMENTAL ILLUSTRATIONS

The sine and cosine functions are two identical trigonometric functions except of a phase shift of $\pi/2$. Thus, we are attempted to state that the Sine and Cosine Fresnel transforms show very

similar, not to say identical, behaviors. The illustrations presented in this section are conceived to explore whether the Sine and Cosine transforms show some distinct behaviors.

Let us consider a binary lens, namely a Fresnel zone plate [1] having two phase levels 0 and □ (Fig. 3a). If the first radius of the Fresnel zone plate is r_1, then its focal length is: $f = r_1^2 / \lambda$. Figure 3b points out the diffraction pattern in the back focal plane of the binary lens. Thus Figure 3b presents the result of the Fresnel transform applied at $z=f$. Theoretically, light focused into the focal point could not exceed $\eta=\text{sinc}(1/2) \cong 40.53\%$ of the light transmitted by the lens since this diffractive element is binary [12]. We notice that $\text{sinc}(\alpha) = \sin(\pi\alpha)/(\pi\alpha)$.

Figures 3c and 3d present the results of the Sine and Cosine transforms respectively, observed in the back focal plane of the binary lens. Figure 3c shows that most of the light, incident to the binary lens, is focused into the focal point with an efficiency of 39%, which is slightly smaller than 40.53%. However, Figure 3d does not show the same behavior. Only a very small part of the incident light (<1%) is focused into the central point of the focal plane. It means that the Sine Fresnel transform shows the converging behavior of the wavefront just behind a binary lens (real distribution), whereas the Cosine Fresnel transform does not.

6. DISCUSSION

To explain the simulation results of Figures 3c and 3d, let us look at the kernels of the Sine and Cosine Fresnel transforms which are expressed by Equations (6) and (5) respectively. The kernel of the Cosine Fresnel transform $f_C(x,z) = \cos(\pi x^2 / \lambda z)$ is the real part of the Fresnel kernel $f_k(x,z) = \exp(j\pi x^2 / \lambda z)$, which is nothing but the transmittance of a diverging wavefront $f_k(x,-z) = \exp(-j\pi x^2 / \lambda z)$ (Fig. 4). Besides, the Cosine Fresnel kernel $f_C(x,z)$ is also the real part of the converging wavefront (Fig. 4), yielding: $f_C(x,-z)=f_C(x,z)$. Thus, the Cosine Fresnel kernel is neutral in terms of convergence or divergence.

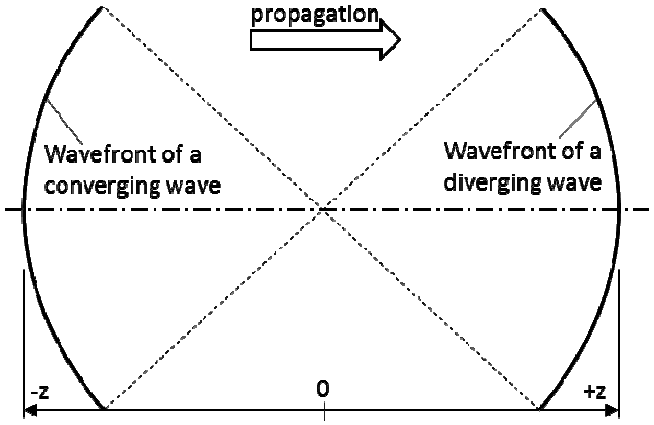

FIGURE 4: Converging and Diverging Wavefronts.

In contrast to the Cosine Fresnel kernel, the Sine Fresnel kernel is sensitive to the direction of propagation (backwards or forwards): $f_S(x,-z)=-f_S(x,z)$. Thus, Sine Fresnel transform is sensitive to the converging or diverging behavior of the wave, represented in our case by a binary real distribution. This explains the observations on Figures 3c and 3d.

For a given initial input distribution $h(x,0)$, that is real, One can obtain the Cosine or Sine Fesnel transform by extracting the real or imaginary part of the Fresnel transform. Since until now there is no receiver that is sensitive to phase, extracting the real or imaginary part of a complex field is not straightforward. It requires a complicated system such as digital or analog holography. In this

case, a hologram is required and the Cosine Fesnel transform is general obtained in two steps: recording hologram then reading it. We propose a less complicated system where you only need to place your object in the optical setup and observe the result on the Camera placed in the output plane.

7. CONCLUSION

In conclusion, two novel transforms called Sine and Cosine Fresnel Transforms were advanced. Moreover, two variants of their optical implementation are presented. The advantage of optics is the high speed of processing of digital signals. These two transforms are very useful in both electronics-based (including DSP and FPGA) or optics-based signal processing. In contrast to the Fresnel transform, both Sine and Cosine Fresnel transforms have the advantage of providing a real result for real input distribution. Except of this difference, all three transforms have similar properties and therefore the same domain of application. Since the Fresnel transform is also the optical version of the fractional Fourier transform, both Fresnel transform and the two proposed transforms, namely the Sine and Cosine Fresnel Transform, show the same properties as the fractional Fourier transform. In that sense, the Sine and Cosine Fresnel transforms may be respectively regarded as the fractional Sine and Cosine transforms, which are more general than the Sine and Cosine transforms. The Sine and Cosine Fresnel transforms may be used in all applications where the Sine and Cosine transforms are applied. However, the former transforms offers an additional degree of freedom which is the propagation distance z.

Although derived from the same transform, namely the Fresnel transform, and the only mathematical difference lies in using the cosine or the sine function, the Sine and Cosine Fresnel transforms show some distinct behaviors. The Sine Fresnel transform is sensitive to the converging or diverging behavior of the wave, represented by a binary real distribution, whereas the Cosine Fresnel transform is neutral in that sense.

As mentioned above, in a future work will explore properties of the Sine and Cosine Fresnel transform including self-imaging related properties. The limitations of the optical implementation will be also explored, and especially: limits of z, tolerance interval of z, tolerance interval of the $\lambda/2$ plate.

We will also explore how to use these two transforms in compression, cryptography and steganography, with both variants: fully digital approach or digital and optical approach.

8. REFERENCES

[1] J. W. Goodman, "*Introduction to Fourier optics*", Roberts & Company Publishers; 3rd Revised Ed, 2005.

[2] V. Namias, "*The fractional order Fourier transform and its application to quantum mechanics*", J. Inst. Appl. Math. , vol 25, pp 241–265, 1980.

[3] D. H. Bailey and P. N. Swarztrauber, *"The fractional Fourier transform and applications,"* SIAM Review, vol 33, pp 389-404, 1991.

1. Bhandari and P. Marziliano, *"Sampling and reconstruction of sparse signals in fractional Fourier domain,"* IEEE Signal Processing Letters, 17, pp 221–224, 2010.

[4] Hong-yi Fan and Li-yun Hu, "*Optical transformation from chirplet to fractional Fourier transformation kernel"* (2009), http://www.arxiv.org/abs/0902.1800. [Feb. 9, 2015]

[5] P. Pellat-Finet, *"Fresnel diffraction and the fractional-order Fourier transform,"* Opt. Lett. , vol 19, pp 1388 – 1390 (1994).

[6] D. Mendlovic and H. M. Ozaktas, *"Fractional Fourier transformations and their optical implementation. I,"* J. Opt. Soc. Am. A, vol 10, pp 1875–1881, 1993.

[7] M. Born and E. Wolf , *"Principles of Optics"*, Pergamon Press, New-York, 1964.

[8] Papoulis, *"Pulse compression, fiber communications, and diffraction: a unified approach,"* J. Opt. Soc. Amer. A, vol 11, pp 3-13, 1994.

[9] J. Azaña and S. Gupta, *"Complete family of periodic Talbot filters for pulse repetition rate multiplication",* Opt. Express, vol 14, pp 4270-4279, 2006.

[10] H. Hamam. *"Talbot imaging and unification"*, Applied Optics - Information Processing. vol 42, pp 7052-7059, 2003.

[11] H. Hamam and J. L. de Bougrenet de la Tocnaye. *"Efficiency of programmable quantized diffractive phase elements"* Pure and Applied Optics, vol 5, pp 389-403, 1996.

INSTRUCTIONS TO CONTRIBUTORS

The *International Journal of Image Processing (IJIP)* aims to be an effective forum for interchange of high quality theoretical and applied research in the Image Processing domain from basic research to application development. It emphasizes on efficient and effective image technologies, and provides a central forum for a deeper understanding in the discipline by encouraging the quantitative comparison and performance evaluation of the emerging components of image processing.

We welcome scientists, researchers, engineers and vendors from different disciplines to exchange ideas, identify problems, investigate relevant issues, share common interests, explore new approaches, and initiate possible collaborative research and system development.

To build its International reputation, we are disseminating the publication information through Google Books, Google Scholar, Directory of Open Access Journals (DOAJ), Open J Gate, ScientificCommons, Docstoc and many more. Our International Editors are working on establishing ISI listing and a good impact factor for IJIP.

The initial efforts helped to shape the editorial policy and to sharpen the focus of the journal. Started with Volume 9, 2015, IJIP will be appearing with more focused issues. Besides normal publications, IJIP intends to organize special issues on more focused topics. Each special issue will have a designated editor (editors) – either member of the editorial board or another recognized specialist in the respective field.

We are open to contributions, proposals for any topic as well as for editors and reviewers. We understand that it is through the effort of volunteers that CSC Journals continues to grow and flourish.

LIST OF TOPICS

The realm of International Journal of Image Processing (IJIP) extends, but not limited, to the following:

- Architecture of imaging and vision systems
- Character and handwritten text recognition
- Chemistry of photosensitive materials
- Coding and transmission
- Color imaging
- Data fusion from multiple sensor inputs
- Document image understanding
- Holography
- Image capturing, databases
- Image processing applications
- Image representation, sensing
- Implementation and architectures
- Materials for electro-photography
- New visual services over ATM/packet network
- Object modeling and knowledge acquisition
- Autonomous vehicles
- Chemical and spectral sensitization
- Coating technologies
- Cognitive aspects of image understanding
- Communication of visual data
- Display and printing
- Generation and display
- Image analysis and interpretation
- Image generation, manipulation, permanence
- Image processing: coding analysis and recognition
- Imaging systems and image scanning
- Latent image
- Network architecture for real-time video transport
- Non-impact printing technologies
- Photoconductors

- Photographic emulsions
- Prepress and printing technologies
- Remote image sensing
- Storage and transmission
- Photopolymers
- Protocols for packet video
- Retrieval and multimedia
- Video coding algorithms and technologies for ATM/p

CALL FOR PAPERS

Volume: 9 - **Issue: 3**

i. Submission Deadline : May 31, 2015 **ii. Author Notification:** June 30, 2015

iii. Issue Publication: July 2015

CONTACT INFORMATION

Computer Science Journals Sdn BhD

B-5-8 Plaza Mont Kiara, Mont Kiara

50480, Kuala Lumpur, MALAYSIA

Phone: 006 03 6204 5627

Fax: 006 03 6204 5628

Email: cscpress@cscjournals.org

CSC PUBLISHERS © 2015
COMPUTER SCIENCE JOURNALS SDN BHD
B-5-8 PLAZA MONT KIARA
MONT KIARA
50480, KUALA LUMPUR
MALAYSIA

PHONE: 006 03 6204 5627
FAX: 006 03 6204 5628
EMAIL: cscpress@cscjournals.org